Chair I of Technical Chemistry
Department of Chemistry
Technical University of Munich

Process simulation with serially arranged reactor modules for the production of solar hydrocarbons

Simulation eines Prozesses mit seriell angeordneten Reaktormodulen zur Produktion solarer Kohlenwasserstoffe

Master's Thesis

Student: B.Sc. Michael Mirkes
Supervisor TUM: Prof. Dr.-Ing. Kai-Olaf Hinrichsen
Supervisor External: M.Sc. David Brust
Date of Submission: 20.11.2022

Institute for Future Fuels
Deutsches Zentrum für Luft- und Raumfahrt (DLR)

Restriction Note

The paper contains confidential information of Deutsches Luft- und Raumfahrtzentrum and may only be made accessible to the employees of TUM who are involved in the examination procedure. A publication of the thesis until (date November 21, 2023) is excluded and the inspection of the thesis by other persons requires an explicit permission of the author and the company.

Acknowledgments

Ich bedanke mich bei David Brust, Michael Wullenkord und dem Institute for Future Fuels des Deutschen Luft- und Raumfahrzentrums sowie Herrn Prof. Dr.-Ing. Hinrichsen von der TU München für die Betreuung meiner Masterarbeit.

Abstract

The FlowPhotoChem project aims to produce ethylene from carbon dioxide and water using three types of reactors and concentrated solar energy. The first reactor concept is a photovoltaic module that is fully electrical and thermally integrated in an electrolyser cell, called photo-electrochemical reactor. The second reactor, called photocatalytic reactor, uses concentrated solar irradiation and photo-active catalysts. The third one is an electrochemical reactor to produce value-added products, in case of this work ethylene. The reactors are serially arranged in two process variants to produce ethylene. The production target is 150 kg/a. The objective of this work is to extend and improve the models for the process simulation of the process variants using Aspen Custom Modeler® . Parameter fits using the current models for the electrochemical module of the reactor are performed. The temperature dependency for the equations of the electrochemical reactor is introduced. For the model of the photocatalytic reactor which is used in the process simulation, an extensive literature review was performed with respect to the reaction mechanism and photocatalytic reaction rates. The photocatalytic reactor is closely investigated using OpenFOAM® to determine the flow behavior of the reactor. Gas separation technologies are assessed and compared. An electrolyser using the parameters from the parameter fit is implemented for the electrochemical reactor module. The resulting reactor modules are implemented in Aspen Custom Modeler® for the process simulation of the two production variants. For each production variant a current state flowsheet showing the current production from the laboratory scaled reactors and a target flowsheet matching the ethylene production target which is 150 kg/a is created in order to determine the linear scaling factors for each reactor in each process variant. Each flowsheet is implemented such that the structure of the flowsheet remains unchanged if the performance or the dimension of the reactors is changed. Lastly, the heat integration potential is analyzed. During the analysis, a variable applicable code interface between Aspen Custom Modeler® and Aspen Energy Analyzer® is implemented.

Contents

List of Figures

List of Tables

List of Source Codes

Nomenclature

Latin Symbols

a	Activity	
$a_1 - a_7$	Nasa7 coefficients	-
b	Van der Waals parameter	-
b	Fitting paramter Phenomenological, Piecewise	V
c	Concentration	mol/m^3
c	Speed of light	m/s
c^*	Concentration near the surface	mol/m^3
c^{0*}	Concentration in the bulk phase	mol/m^3
c_{cp}	Heat capacity	J/(mol K)
C_f	Skin friction	-
D	Diffusion coefficient	m^2/s
D'	Overall diffusion coefficient in multicomponent system	m^2/s
D^{eff}	Effective diffusion coefficent	m^2/s
d_{p}	Particle diameter	m
E	Energy	J
E_{a}	Activation energy	J/mol
E_{g}	Bandgap energy	eV
E_{A}	Activation energy	J/mol
F	Faraday constant	s A/mol
f	Friction coefficient	-
G	Gibbs Free Energy	J
g	Molar Gibbs Free Energy	J/mol
H	Enthalpy	J
h	Molar enthalpy	J/mol
$h^0_{f,i}$	Molar enthalpy of formation	J/mol
h	Planck constant	m^2/(kg s)
Δh_{rxn}	Change of enthalpy of a reaction	J/mol

I	Current	A
j	Current density	A/m^2
j_L	Current density limit from activation overpotential in the phenomenological and piecewise model	A/m^2
$\hat{j}_L$	Current density limit from concentration overpotential	A/m^2
J_L	Load current density	A/m^2
J_{sc}	Short circuit current density	A/m^2
$j_{transport}$	Mass Transport	A/m^2
J_0	Diode reverse saturation current density	A/m^2
j_0	Exchange current density	A/m^2
L	Length	m
$\bar{n}$	Diode ideality factor	-
N	Number of molecules	-
N_S	Number of serial PV cells	-
N_S	Number of parallel PV cells	-
$\dot{n}$	Mole flow	mol/s
p	Pressure	N/m^2-
P	Power	W
q	Fundamental charge	°C
R	Ideal gas constant	J/(mol K)
r	Rate of reaction	mol/s
$R_{s,i}$	Series resistance	Ω
r_0	Impenetrable core of radius of a particle	m
S	Entropy	J/K
s	Molar entropy	J/(mol K)
$s^0_{f,i}$	Molar entropy of formation	J/(mol K)
Δs_{rxn}	Change of entropy of a reaction	J/(mol K)
S, S_ϕ	Source	
T	Temperature	K
t	Time	s
U	Internal Energy	J
u	Molar Internal Energy	J/mol
u	Velocity	m/s
u_∞	Free stream velocity	m/s
u_τ	Friction velocity	m/s
V	Volume per gas molecule	m^3
v	Volume per gas molecule	m^3
V	Voltage	V

y	Molar fraction in gas phase	-
$\hat{y}$	Absolute wall distance	m
y^+	Dimensionless wall distance	-
z	Dumber of electrons	-

Greek Symbols

α	Charge transfer coefficient	-
α	PV material constant	eV/K
β	PV material constant	K
Γ	Diffusivity	m^2/s
γ	PV material constant	-
ε	Lennard-Jones potential well depth	ergs
ε_{cat}	porosity of a catalyst	-
η	Dynamic viscosity	kg/(m s)
η	Overpotential	V
κ	PV material constant	$A/(m^2\,K^4)$
λ	Wave length	m
μ	Chemical Potential	J, J/mol
$\bar{\mu}$	Molecular mass	kg/mol
ν	Stoichiometric coefficients	-
ν	Frequency	1/s
ν	Kinematic viscosity	m^2/s
ϕ	Scalar transport property	
χ	Molar fraction in liquid	-
ρ	Density	kg/m^3
σ	Lennard-Jones diameter	Å
τ_{cat}	Totuosity of a catalyst	-
Ω	Collision integral	-
Ω	Non-ideality correction factors phenomenological model	Ωcm
Ω^*	Non-ideality correction factors piecewise model	$\Omega^2 cm^2$

Superscript

0	Standard State

Subscript

act	Activation
an	Anode
cat	Cathode
conc	Concentration
el	Electrical
f	Formation
i	Species index
L	Load
l	Limit
p	Pressure
P	Product
R	Reactant
rxn	Reaction
sc	Short circuit

Dimensionless Numbers

Pe	Pėcelt number
Pr	Prandtl number
Re	Reynolds number
Sc	Schmidt number

Abbreviations

ACM	Aspen Custom Modeler®
ASR	Area Specific Resistance
CO2R	Carbon Dioxide Reduction
COR	Carbon Monoxide Reduction
CFD	Computational Fluid Dynamics
DIPA	Diisopropanolamine
EC	Electrochemical
EC-COR	Electrochemical Carbon Monoxide Reduction
ELECNRTL	Electrolyte Non-Random-Two-Liquids
IUPAC	International Union of Pure and Applied Chemistry
KOH	Potassium Hydroxide

MEA	Monoethanolamine
NHE	Normal Hydrogen Electrode
NIST	National Institute of Standards and Technology
PC	Photocatalytic
PEC	Photo-Electrochemical
PEMWE	Proton Exchange Membrane Water Electrolyser
RHE	Reversible Hydrogen Electrode
SHE	Standard Hydrogen Electrode
STP	Standard Temperature and Pressure
VLE	Vapour-Liquid-Equilibrium

1 Introduction

One of the greatest challenges of our time is climate change. This is caused by the emission of climate-damaging gases, which are gases that intensify the greenhouse effect of the earth's atmosphere and thus cause an accelerated rise in temperature. The vast majority of anthropogenic greenhouse gases is carbon dioxide. In Germany, it accounts for 87.1 % of the greenhouse gases released [1]. The energy sector accounted for 84 % of greenhouse gas emissions in Germany in 2021 through the combustion of fossil fuels, and industrial processes were responsible for another 7.5 % [2, 3].

Model calculations predict a possible temperature increase of 1.6 °C to 4.7 °C in the future. An actual increase of more than 2 °C would have serious consequences for the Earth, such as a significant rise in sea level, extreme weather events, or large-scale rainforest dieback. To limit these consequences, 55 nations worldwide pledged in 2015 at the UN Climate Change Conference in Paris to take action to limit the global temperature increase to a maximum of 2 °C above pre-industrial levels. These nations include the European Union and thus Germany. This target can only be achieved if fossil fuels are not used in the future. The German Advisory Council on Global Change already showed in a 2011 report "that a global transformation of energy systems allowing all people to be supplied with modern energy while limiting human-induced global warming to 2 °C is technically possible and economically feasible."[4]. According to the Federal Environment Agency, non-energy consumption accounts for about 8 % of fossil fuels in Germany. The most important consumer here is the petrochemical industry [5]. The goal must be to provide industry with alternatives to the use of petroleum. One of the substances being researched for its "green" production, meaning sustainable by using renewable sources and renewable energy, is ethylene, one of the most important substances in the industry [6]. Processes are currently being developed in industrialized nations to produce ethylene from CO2 and water. These processes are very energy intensive. Economic aspects play a major role for the production of "green" feedstock. Synthesizing ethylene using renewable energy and by recovering CO2 from the air, thus closing the CO2 cycle and avoiding further release of this gas into the atmosphere, is only likely to succeed if the processes used are cost-effective and competitive with the use of petrochemicals. To achieve these goals, the

Institute of Future Fuels in Jülich is a project partner in the FlowPhotoChem [7] project currently conducting experiments with the aim of producing ethylene from carbon dioxide and water.

Introduction to the FlowPhotoChem Project Using carbon dioxide and sunlight, the FlowPhotoChem research initiative is creating new and improved techniques for chemical synthesis. Concentrated solar energy and newly developed catalysts are utilized to convert carbon dioxide and water into high-value products such as ethylene. Ethylene serves as a precursor for plastics, and has a significant potential to replace a large portion of the fossil fuels used today to generate fuels and valuable chemicals. The main obstacles to achieving this are better solar light management, more effective reactors, and more resilient catalysts, which are all addressed by the FlowPhotoChem project. The initiative researches three reactor concepts, the photo-electrochemical, the photocatalytic and the electrochemical reactor concept. The three reactors are serially arranged to produce the desired product. [7].

Objective of this Work The objective of this thesis within the framework of the FlowPhotoChem project is to extend and improve the simulation approaches and models for the three existing reactor models. Currently, an ethylene production target of 150 kg/a is pursued. Part of the work of this thesis is the implementation of process simulations that illustrate the current laboratory scale of the reactors and to scale the process simulation to match the production target. In order to accurately depict the performance of each reactor, parameter fits are performed as part of this work to model the serially arranged process variants. The necessary utilities and process engineering, such as gas separation technologies are developed in this thesis to match the requirements of each reactor when they are serially arranged. Finally, this thesis investigates the heat integration potential of the process variants.

2 Theory

In this work, solar power is deployed in three different methods to harvest energy from solar irradiation. The energy is then utilized in serially arranged reactors to synthesize the high value product ethylene from carbon dioxide and water. In the following chapter, firstly the thermodynamic fundamentals necessary for the models used in this work will be examined. Secondly, the working principle and chemical reactions for each reactor will be discussed. Lastly, the necessary principles for the process design and utilities will be presented.

2.1 Fundamentals

2.1.1 Thermodynamics

Gibbs free energy G denotes the energy needed to form a thermodynamic system. It is calculated from the sum of internal energy U and the thermodynamic work to make room for the thermodynamic system pV minus the thermal energy from the environment TS. In the equation (2.2) and (2.3) S denotes the entropy, p the pressure, V the volume, T the temperature and H the enthalpy. If the internal energy U and pressure work pV are greater than the thermal energy TS supplied from the environment, the system can exert thermodynamic work on its environment. Hence, the Gibbs free energy quantifies the maximum amount of non-expansion work a thermodynamic system can perform in a closed system in a fully reversible process [8, 9].

$$G = U + pV - TS \tag{2.1}$$

$$= H - TS \tag{2.2}$$

The differential form of the Gibbs free energy in a closed thermodynamic system can be derived by variation of G [8].

$$\mathrm{d}G = -S\mathrm{d}T + V\mathrm{d}p \tag{2.3}$$

The molar enthalpy of formation $h^0_{f,i}$ quantifies the energy necessary to form one mole of a species i in standard state. The Standard state is defined by the International Union of Pure and Applied Chemistry (IUPAC) as a reference state by convention for the calculation of thermodynamic quantities [10]. For gases, the values are calculated as pure substances using the ideal gas equation and a recommended standard pressure of $10^5\,\mathrm{N/m^2}$. For elements, the standard state is defined in the phase in which the element exists in the most stable allotrope and a pressure of $10^5\,\mathrm{N/m^2}$. For pure substance in a condensed state, the reference state is defined at a pressure of $10^5\,\mathrm{N/m^2}$. For solutions, the standard state is defined at a pressure of $10^5\,\mathrm{N/m^2}$ and solute concentration of 1 M with an infinite-dilution behavior. The temperature is not part of the IUPAC definition of the standard state. Commonly, a temperature of 298.15 K is used to determine the standard state value of a thermodynamic quantity [11]. Standard enthalpies of formation can be obtained from literature and databases, such as National Institute of Standards and Technology. Alternatively, the dependency on temperature can be calculated with the integral over the heat capacity c_{cp} and typically a polynomial expression for the heat capacity.

$$h_{\mathrm{f}} = h^0_{\mathrm{f}} + \int_{T_0}^{T} c_{\mathrm{p}}(T)\,\mathrm{d}T \tag{2.4}$$

The temperature dependence of the molar entropy s_{f} can be calculated similarly.

$$s_{\mathrm{f}} = s^0_{\mathrm{f}} + \int_{T_0}^{T} \frac{c_{\mathrm{p}}(T)}{T}\,\mathrm{d}T \tag{2.5}$$

The change of enthalpy and entropy of a reaction can be calculated as difference of the molar weighted enthalpy and entropy of formation, respectively with the stoichiometric coefficients ν_i for each species i involved in the reaction.

$$\Delta h_{\mathrm{rxn}} = \sum_{\mathrm{i}} \nu_{\mathrm{i}} h_{\mathrm{f,i}} \tag{2.6}$$

$$\Delta s_{\mathrm{rxn}} = \sum_{\mathrm{i}} \nu_{\mathrm{i}} s_{\mathrm{f,i}} \tag{2.7}$$

Substituting these definitions in equation (2.1), the change of Gibbs Free Energy for a reaction can be calculated with equation (2.8)

$$\Delta g = \Delta h - T\Delta s \tag{2.8}$$

The energy necessary to add an infinitesimal change of particle number n_i of a species i to the system is defined as chemical potential μ_i [8].

$$\mu_\mathrm{i} = \left(\frac{\partial G}{\partial n_\mathrm{i}}\right)_{T,p,n_{\mathrm{j}\neq\mathrm{i}}} \tag{2.9}$$

Hence, the chemical potential μ_i characterizes how much the the Gibbs free energy G changes with the number of particles of a species i removed or added to the system [8]. Inter particle forces need to be considered if more than one species is present and describes the deviation from an ideal solution. The chemical potential is related to the activity a, and the effective concentration [12] by the following equation.

$$\mu_\mathrm{i} = \mu_\mathrm{i}^0 + RTln(a_\mathrm{i}) \tag{2.10}$$

For chemical reactions under constant pressure and temperature, the change of the Gibbs free energy can be calculated from the chemical potential and the activities of all species i involved [8].

$$\mathrm{d}G = \sum_\mathrm{i} \mu_\mathrm{i} \mathrm{d}n_\mathrm{i} = \sum_\mathrm{i} (\mu_i^0 + RTlna_\mathrm{i})\mathrm{d}n_\mathrm{i} \tag{2.11}$$

2.1.2 Mass Transfer

Transport of mass can be driven by convection and by diffusion. While the first results from an external force to transport the fluid, the latter is driven by concentration gradients. The two regimes can be distinguished by the dimensionless Pėcelt number. For diffusive mass transfer the quantity is given by ratio of the characteristic length L, the local flow velocity u and the the mass diffusion coefficient D. Alternatively, the Pėcelt number can be expressed as the product of the dimensionless Reynolds number Re and the Schmidt number Sc [8, 13].

$$\mathrm{Pe} = \frac{Lu}{D} = \mathrm{Re\ Sc} \tag{2.12}$$

The Pėcelt number can be calculated from the Reynolds number Re, Schmidt number Sc with the density ρ, and the dynamic viscosity η

$$\mathrm{Re} = \frac{d\rho u}{\eta} \tag{2.13}$$

$$\mathrm{Sc} = \frac{\eta}{\rho D} \tag{2.14}$$

$$\tag{2.15}$$

If the Pėcelt number is much greater than unity, the diffusion time is much greater than the convection time and the diffusive contribution is negligible. It is important to note, that the Pėcelt number for heat and mass transfer can differ and thus, in some cases, diffusion can be neglected in one but not the other conservation equation [14].

2.1.3 Transport Equations

The balance of an infinitesimally small domain can be expressed as [15]

$$\frac{\partial \vec{c}}{\partial t} + \nabla \cdot \bar{j} = S \tag{2.16}$$

After splitting the flux $\bar{j}$ into the convective and the diffusive contribution, this equation can be written as

$$\frac{\partial \vec{c}}{\partial t} + \nabla \cdot (D \nabla \vec{c}) + \nabla \cdot (\vec{u}\vec{c}) = S \tag{2.17}$$

with the concentration vector $\vec{c}$, the time t, the source S

2.1.4 Transport Parameters

For dilute gas mixtures the following equations can be derived from the kinetic theory of gases to calculate the diffusion coefficients. The criteria for a sufficiently diluted gas is met, when the volume per gas particle is much greater than the van der Waals parameter b ($b \ll v$) [16, p. 311] with the volume per particle v, the number of particles N, the average

attraction between particles b, and the impenetrable core of radius r_0 of a particle [16, p. 309].

$$v = \frac{V}{N} \tag{2.18}$$

$$b = \frac{2\pi r_0^3}{3} \tag{2.19}$$

For diffusion in binary systems, the diffusion coefficient can be calculated using the relation derived by Bird, Hirshfelder and Curtiss [17] with the binary diffusion coefficient of the species A and B D_{AB}, the collision integral Ω, the molecular mass $\bar{\mu}$, the Lennard-Jones potential well depth ε, effective Lennard-Jones potential well depth for the collision $\varepsilon_{\mathrm{AB}}$, the Lennard-Jones diameter σ, the effective Lennard-Jones collision diameter σ_{AB}, and the Boltzmann's constant k_{B}.

$$D_{\mathrm{AB}} = \frac{1.883 \cdot 10^{-20} T^{3/2} (1/\bar{\mu}_{\mathrm{A}} + 1/\bar{\mu}_{\mathrm{B}})^{1/2}}{p \sigma_{\mathrm{AB}}^2 \Omega} \tag{2.20}$$

$$\frac{\varepsilon_{\mathrm{AB}}}{k_{\mathrm{B}}} = \left(\frac{\varepsilon_{\mathrm{A}}}{k_{\mathrm{B}}} \frac{\varepsilon_{\mathrm{B}}}{k_{\mathrm{B}}} \right)^{1/2} \tag{2.21}$$

$$\sigma_{\mathrm{AB}} = \frac{\sigma_{\mathrm{A}} + \sigma_{\mathrm{B}}}{2} \tag{2.22}$$

$$\tag{2.23}$$

For many molecules, such as e.g. H_2, H_2O, O_2, CO and CO_2, the parameters for the Lennard-Jones potential well depth ε and collision diameter σ can be found in the Grimech3.0 files [18]. Values for the collision integrals for the Lennard-Jones-(12, 6)-potential can be obtained from Hirschfelder et al. [17] or Klein and Smith [19]. Since the collision integral is dependent on the temperature, table 2.1 only lists the potential well depth and collision diameter.

Table 2.1: Transport parameters for selected species obtained from the Gri-Mech 3.0 [18].

Species	$\varepsilon/k_{\mathrm{B}}$	σ
CH_4	141.400	3.746
CO	98.100	3.650
CO_2	244.000	3.763
H_2	38.000	2.920
H_2O	572.400	2.605
O_2	107.400	3.458

The overall diffusion coefficient of a multicomponent system can then be calculated with the molar fractions in the gas phase y [20].

$$D'_{\mathrm{A}} = \frac{1 - y_{\mathrm{A}}}{\frac{y_{\mathrm{B}}}{D_{\mathrm{AB}}} + \frac{y_{\mathrm{C}}}{D_{\mathrm{AC}}} + \ldots} \tag{2.24}$$

For diffusion in porous media, such as catalysts and electrodes of electrolysers, the porosity of the catalyst $\varepsilon_{\mathrm{cat}}$ and the tortuosity of the catalyst τ_{cat} are used to calculate an effective diffusion coefficient from the theoretical diffusion coefficient [21].

$$D_{\mathrm{i}}^{\mathrm{eff}} = D_{\mathrm{i}} \frac{\varepsilon_{\mathrm{cat}}}{\tau_{\mathrm{cat}}} \tag{2.25}$$

2.2 Reactors

The FlowPhotoChem project aims to produce high value chemicals using carbon dioxide. The project uses three reactor concepts, the photo-electrochemical (PEC) reactor which is a coupled photovoltaic (PV) module and an electrolyser to produce hydrogen from water splitting, the photo-catalytic reactor which is used to reduce carbon dioxide to carbon monoxide via the reverse water gas shift reaction (RWGS) in the presence of a photo-active catalyst, and the electrochemical carbon monoxide reduction (EC-COR) reactor which is used to convert the produced carbon monoxide to the desired products. In this work, the desired product is ethylene. The following chapters introduce the theory to simulate all modules of the process.

2.2.1 Photovoltaic Cell and Module

For the utilization of solar energy solar cells are deployed. In these cells the incoming photon can excite an electron and move it from a valence band to a conduction band, if the energy of the photon is greater than the band gap energy E_{g} between both energy levels [22, p. 44]. The relation is calculated with the Planck constant $\hbar$, the frequency of the photon ν_{Photon} and the corresponding frequency ν_0 to the electron transition from the valence to the conduction band [23].

$$\hbar \nu_{\mathrm{Photon}} \geq \hbar \nu_0 = E_{\mathrm{g}} \tag{2.26}$$

The electrons transferred from the valence band to the conduction band are then available as charge carriers. The current-voltage performance characteristic of semiconductor photovoltaic cells can be well described by an equivalent circuit model of photo-diodes [24, p. 50] where I_s is the dark current which can be strongly dependent on the temperature and material constants, I_l the light current , q the elementary charge, and V the voltage.

$$I(\mathrm{V}) = I_l - I_s \left(\exp\left(\frac{qV}{k_B T_2} \right) - 1 \right) \tag{2.27}$$

The dark current is temperature- and bandgap-dependent. Thus, the current-voltage characteristic is a function of the bandgap energy. The electrical power available is also dependent on the bandgap energy E_g of the semiconductor, since the electrical power is given by the product of the current I and the voltage V [25].

$$P_{el} = I\,V \tag{2.28}$$

Hence, alloy compositions of different semiconductor materials are layered to maximize the efficiency of a solar cell since per photon only one electron is excited [22, p. 62]. This is a common hypothesis on photovoltaic cell calculations. Photons with shorter wavelength can be used to excite electrons in materials with larger bandgaps. Thus, the overall performance of the cell an be improved if more than one semiconductor is used. For this work, an InGaP/InGaAs/Ge triple-junction photovoltaic cell is used. For the performance modeling of photovoltaic cells used in this work, the effects of operating temperature and the concentration of solar irradiation should be considered carefully and can be related with semi-empirical cell models [26]. The temperature dependence of the band gap energy for a single junction can be calculated with the material constants $E_g(0)$, α , β [27, 28].

$$E_g = E_g(0) - \frac{\alpha T^2}{T + \beta} \tag{2.29}$$

The bandgab energy for a single junction made up from an alloy composition $A_{1\text{-}x}B_x$, eg. for the InGaP junction consisting of the elements In, Ga and P can be calculated by linear combination of the individual elements' bandgap energies. f_{Eg} denotes the band gap correction factor for each junction [29].

$$E_g(A_{1\text{-}x}B_x) = (1-x)E_g(\mathrm{A}) + xE_g(\mathrm{B}) - x(1-x)f_{Eg} \tag{2.30}$$

The voltage of each junction is calculated using the diode ideality factor $\bar{n}_\mathrm{i}$, short circuit density J_sc, the diode reverse saturation current density J_0, the load current density J_L, the series resistance $R_\mathrm{s,i}$ and the area A [26].

$$V_i = \frac{\bar{n}_\mathrm{i} k_\mathrm{b} T}{q} \ln\left(\frac{J_{sc} - J_l}{J_{0,i}} + 1\right) - J_\mathrm{l} A R_\mathrm{s,i} \tag{2.31}$$

The overall voltage of the triple junction cell is calculated with the sum of all single junctions [26].

$$V_{cell} = \sum_{i=1}^{3} V_\mathrm{i} \tag{2.32}$$

The diode reverse saturation current I_0 for a junction i is calculated using the area A and temperature T of the PV cell, and the material constants κ_i, γ_i, and n_i

$$I_0(i) = \kappa_\mathrm{i}\left(T_\mathrm{PV}^{(3+\gamma_\mathrm{i}/2)} \exp\left(\frac{-E_\mathrm{g,junction,i}}{n_\mathrm{i} k_\mathrm{B} T_\mathrm{PV}}\right)\right) \tag{2.33}$$

The maximum load current I_L is given by the minimum of the short circuit currents I_sc of all junctions in the PV cell and can be strongly dependent on temperature [26, 30].

$$I_\mathrm{L} = Min(I_\mathrm{sc}) \tag{2.34}$$

Since the current and voltage output of individual cells are limited, cells are connected together to form modules. The total current and voltage of a solar panel string depends on the electrical wiring of the number of serially N_s and number of parallel N_p connected cells.

$$V_\mathrm{String} = N_\mathrm{s}\, V_\mathrm{cell} \tag{2.35}$$

$$I_\mathrm{String} = N_\mathrm{p}\, J_\mathrm{cell}\, A_\mathrm{cell} \tag{2.36}$$

2.2.2 Electrolyser Cell and Module

The principle working mechanism of an electrolyser is two electrodes, anode and cathode, which are separated by an ion-permeable membrane. An external voltage is applied between the two electrodes to initiate an electrochemical reaction at the surface of the

electrode. The overall reaction can be split into the two half cell reactions, the oxidation reaction that loses electrons and the reduction reaction that gains electrons[31].

$$\mathrm{A} \longrightarrow \mathrm{A}^{+} + \mathrm{e}^{-} \tag{R1}$$

$$\mathrm{B} + \mathrm{e}^{-} \longrightarrow \mathrm{B}^{+} \tag{R2}$$

The overall voltage resulting from the Redox reaction is called Redox potential and is the minimum electrical work that is required in an electrolyser to operate. The relation between the rate at which products form and the overall current in the electrolyser cell is given by Faraday's second laws of electrolysis [31]. I denotes the current, r the molar rate of change of a substance and n the number of electrons transferred.

$$I = rzF \tag{2.37}$$

In electrolysers, electrical energy is used to prompt electrochemical, non-spontaneous reactions ($\Delta g_{\mathrm{rxn}} > 0$). Since the Gibbs Free energy change of the reaction quantifies the work needed for the electrochemical reaction, the corresponding reversible voltage required to prompt the reaction can be calculated with equation (2.38) for standard conditions [8] and the Faraday constant F.

$$E^{0} = -\frac{\Delta \hat{g}^{0}_{\mathrm{rxn}}}{nF} \tag{2.38}$$

As previously shown in the fundamentals, the change of the Gibbs free energy with the temperature is given by the entropy S (see equation (2.3)) and with the particle number n_i is given by the chemical potential μ. Using equation 2.11 the reversible voltage dependence on the temperature and concentration can be deduced [8].

$$E_{rev} = E^{0} + \frac{\Delta s}{nF}(T - T_0) - \frac{RT}{nF}\frac{\prod a^{\nu_i}_{products}}{\prod a^{\nu_i}_{reactants}} \tag{2.39}$$

The overall electrolyser performance is affected by the thermodynamic potential and three major loss types, the ohmic losses η_{ohmic}, activation losses η_{act}, and mass transfer losses [8].

$$V = E_{thermo} + \eta_{act} + \eta_{ohmic} + \eta_{conc} \tag{2.40}$$

Figure 2.1 shows the contribution of three major overpotentials as a function of the current density j.

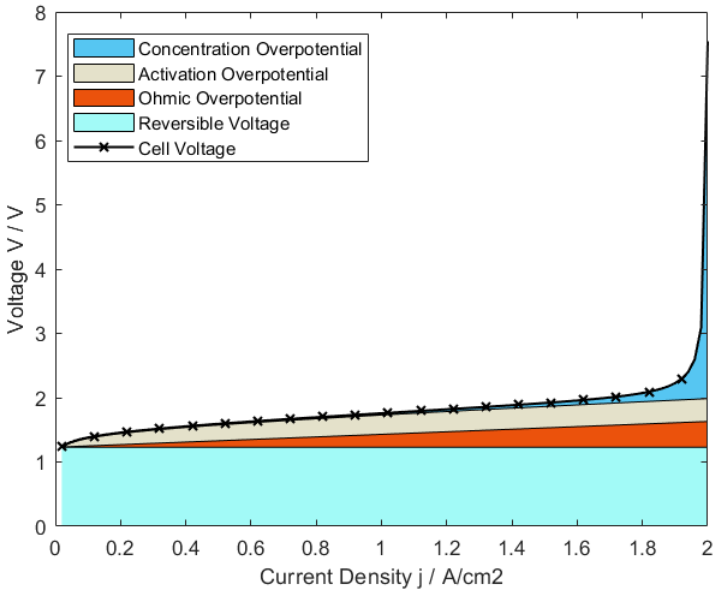

Figure 2.1: Current-Voltage characteristic for three major loss contributions ohmic, activation and concentration overpotential with hypothetical parameter.

Ohmic Overpotential The transportation of charge is subject to losses from intrinsic resistance, such as electric and ionic resistance. In general, the ionic resistance is usually much greater than the electric resistance [8, p. 128]. The ohmic overpotential η_{ohmic} is calculated with the current density j, the electrical resistance R_{elec}, the ionic resistance R_{ionic}, the area of the cell A and the area surface resistance ASR [8].

$$\eta_{\text{ohmic}} = jA(R_{\text{elec}} + R_{\text{ionic}}) = j\ \text{ASR} \tag{2.41}$$

Activation Overpotential The rate of reaction in which an electrochemical reaction occurs is related to the activation barrier. The size of the activation barrier can be manipulated if greater values of cell voltages than the electrochemical potential are supplied. The relation between the activation overpotential η_{act} and the current density j is calculated with the Butler-Volmer equation with the number of electrons transferred n, the reactant R and product P concentrations of the rate-limiting species in the bulk phase c^{0*} and near the surface c^*, the current density at standard concentration j_0, the universal gas constant R and the charge transfer coefficient α [8].

$$j = j_0 \left(\frac{c_{\text{R}}^*}{c_{\text{R}}^{0*}} \exp\left(\frac{\alpha n F \eta}{RT} \right) - \frac{c_{\text{P}}^*}{c_{\text{P}}^{0*}} \exp\left(\frac{-(1-\alpha) n F \eta}{RT} \right) \right) \tag{2.42}$$

The Butler-Volmer equation is a valid approximation for most single-electron transfer mechanisms or if one intrinsically much slower rate-determining step dominates the reaction mechanism[8, p. 92]. Equation (2.42) can be further simplified if the activation overpotential is either very small ($\eta_{act} < 15mV$ at room temperature) [8].

$$j = j_0 \frac{nF\eta_{\text{act}}}{RT} \tag{2.43}$$

or the activation overpotential is large ($\eta_{act} > 50-100mV$ at room temperature) [8].

$$j = j_0 \exp^{\frac{\alpha nF\eta_{\text{act}}}{RT}} \tag{2.44}$$

The latter equation is known as the Tafel equation if rearranged for the activation overpotential.

$$\eta_{\text{act}} = -\frac{RT}{\alpha nF}\ln j_0 + \frac{RT}{\alpha nF}\ln j \tag{2.45}$$

$$\eta_{act} = a + b\log j \tag{2.46}$$

Since the activation overpotentials used in this work are always much greater than the threshold value to maximize the production of ethylene, the Tafel equation is used exclusively in different forms throughout this thesis.

Concentration Overpotential With further increase in the values of cell voltage applied, the reaction rate increases. If the reaction rate becomes greater than the rate at which reactants can be supplied to the surface of the electrode where the reaction occurs, the regime switches from a kinetically limited to a transport limited regime. Although sufficiently high bulk concentration can be assured through convective mixing by increasing the velocity of the gas stream, a concentration gradient in the viscous sublayer will remain since the velocity is very small and zero at the phase boundary between the fluid and the electrode. This layer is also called diffusion layer, since the dominant transport is diffusion driven in contrast to the bulk phase, where convective transport is dominant. To calculate the concentration overpotential, the mathematical expression needs to satisfy the conditions for the current density limit from concentration losses $\hat{j}_{\text{L}}$ [32]

$$\eta_{conc} \begin{cases} 0 & \text{if} \quad j \ll \hat{j}_{\text{L}} \\ \nexists & \text{if} \quad j \geq \hat{j}_{\text{L}} \\ \infty & \text{if} \quad j \approx \hat{j}_{\text{L}} \end{cases} \tag{2.47}$$

Garcia-Navarro et al. proposed the following equation [32]

$$\eta_{\text{conc}} = \frac{RT}{zF} \ln\left(\frac{1}{1-\frac{j}{j_{\text{L}}}}\right) \tag{2.48}$$

O'Hayre et al. [8] suggested a adaption using the the charge transfer coefficient α.

$$\eta_{\text{conc}} = \frac{RT}{zF}\left(1+\frac{1}{\alpha}\right) \ln\left(\frac{1}{1-\frac{j}{j_{\text{L}}}}\right) \tag{2.49}$$

Since throughout this thesis only very limited experimental data suitable for the study of mass transport effects on cell performance was available, the model which will later be introduced (see chapter 4.2) only accounts for ohmic overpotential losses and activation potential losses. This should be considered when the flowsheet will be optimized. The upper bound four the current density of the electrolyser should match the maximum current density at which experimental data has been available.

2.2.3 Photo-Electrochemical Reactor

2.2.4 Photocatalysis

In the previous chapter it was discussed how applying an external electrical cell voltage can prompt a redox reaction. However, redox reactions can also occur if a photon-excited semiconductor with a bandgap energy greater than the redox potential provides the electrons for the reaction. Electrons in semiconductors can either be present in an unexcited (valence band) or excited state (conduction band). Each band is characterized by an energy range. Electrons must be in either band because electronic states between these two bands do not exist in the case of a semiconductor. The difference between the upper bound of the valence band and the lower bound of the conduction band is referred to as the energy gap or bandgap. In order to promote a valence electron from the valence band to the conduction band, the energy that is provided must be greater or at least equal to the band gap. [33] The band gap energy and the electron density distribution are both dependent on temperature [28]. With increasing temperature, more valance electrons are excited to the conduction band and hence can move freely and participate as charger carriers. The distribution of electrons between both bands is characterized by the Fermi-Dirac

distribution [34]. However, electrons can also be (shortly) excited from the valence band to the conduction band by the interaction with electromagnetic radiation (photon) leaving a positively charged electron-hole. The corresponding wavelength λ_c of the photon can be calculated from the speed of light in vacuum c, the Planck constant h and the band gap energy E_g [33, 34, p.47].

$$\lambda_c = \frac{ch}{E_g} \tag{2.50}$$

Semiconductors with a greater number of electromagnetically produced electron-hole pairs than thermally produced pairs are called photoconductors [33]. This effect is utilized in photo-catalytic reactors. For a typical photocatalytic reaction three components must be present [35]

(1) an emitted photon with an appropriate wavelength
(2) a catalytic surface
(3) a strong oxidizing agent

Typically, a semiconductor is combined with a metal co-catalyst, that transfers the electromagnetically excited electron from the semiconductor to an acceptor molecule. The generated electrone-hole acts as a strong oxidizing agent and accepts an electron from a donor molecule. This results in the desired Redox-reaction [36]. However, this pathway competes with electron-hole and electron recombination. After the separation of charges two competing (volume recombination and surface recombination) pathways can decrease the efficiency of the photo catalyst [35, 36].

The tendency of molecular orbitals to accept/donate electrons is quantified by their redox potential. For the reduction reaction, the conduction band edge of the photocatalyst must be greater than the lowest unoccupied molecular orbital (LUMO). For the oxidation process the valence band edge must be smaller than the highest occupied molecule orbital (HOMO). On the other hand, the band gap must be as small as possible to increase the absorption efficiency through shifting the critical wavelength in the visible range (see equation (2.50)). This poses very strict restrictions on the semiconductor used as photocatalyst. The photo-reduction of CO_2 can result in a variety of products (E_0 vs Normal

Hydrogen Electrode (NHE) at pH 7) [36].

$$CO_2 + 2H^+ + 2e^- \longrightarrow HCOOH \qquad E^0_{redox} = -0.61V \qquad \text{(R3)}$$
$$CO_2 + 2H^+ + 2e^- \longrightarrow CO + H_2O \qquad E^0_{redox} = -0.53V \qquad \text{(R4)}$$
$$CO_2 + 4H^+ + 4e^- \longrightarrow HCHO + H_2O \qquad E^0_{redox} = -0.48V \qquad \text{(R5)}$$
$$CO_2 + 6H^+ + 6e^- \longrightarrow CH_3OH + H_2O \qquad E^0_{redox} = -0.38V \qquad \text{(R6)}$$
$$CO_2 + 8H^+ + 8e^- \longrightarrow CH_4 + 2H_2O \qquad E^0_{redox} = -0.24V \qquad \text{(R7)}$$
$$2H^+ + 2e^- \longrightarrow H_2 \qquad E^0_{redox} = -0.41V \qquad \text{(R8)}$$

2.2.5 Absorption Column

In absorption columns, the gas phase feed is brought into contact with a fluid (absorbent) to selectively absorb components (absorbate) of the gas mixture. Absorption towers can feature either tray or packed columns to maximize the surface area of the absorbent and thus improve the absorption rate. The type of column used depends on the diameter of the column, the capacity factor and the turndown ratio. The selective mass transfer with phase transition can occur from physical or chemical absorption. In this work, a counter flow absorption column has been implemented using a specified number of vapor-liquid-equilibrium calculations with an electrolyte physical property model. [37–39]

2.3 Optimization

The objective of an optimization problem is to find the overall best solution such that the set of parameters, called decision or design variables $\vec{x}$ best fits the optimization set in the response space. The function $f(\vec{x})$ that is set to be minimized is called the cost function or objective function [40, p. 5].

$$\min f(\vec{x}) \qquad (2.51)$$

To determine the overall fitness of the model, the deviation between the responses Y^{calc} of the design parameters x and the observations Y^{exp} need to be quantified with an error function. Equation (2.52) shows a typical error function [41, p. 4].

$$f(x) = \frac{1}{n_{res}} \left\| (Ax - y)^2 \right\| \tag{2.52}$$

However, different optimization problems can require different error functions and the choice of the error function should be justified with the optimization problem presented. The optimization problem can be either unconstrained or subject to equality-constrained and/or inequality-constrained lower $\vec{l}_{\text{b}}$ and upper $\vec{u}_{\text{b}}$ boundaries

$$\vec{l}_{\text{b}} \leq \vec{x} \leq \vec{u}_{\text{b}} \tag{2.53}$$

$$\vec{l}_{\text{b}} \leq c(\vec{x}) \leq \vec{u}_{\text{b}} \tag{2.54}$$

$$\tag{2.55}$$

The space that fulfills these requirements is called feasible domain.

As experimental results are prone to errors, it is important to first characterize the nature of error. A random error is characterized by a high accuracy and a high standard deviation. A systematic error is characterized by the opposite, a low accuracy and a low standard deviation [42]. It should be noted in the following context, that a model fit done by multivariable optimization can only make up for errors of the first type but not for the latter, since the model will be fitted to the systematic error.

In this study, multi-objective equality-constrained, non-linear optimization problems with more than one optimum (multimodal) have been encountered for fitting the used models to experimental data and optimizing the process simulation flowsheet. To solve such problems, different strategies and algorithms can be used.

Gradient-based Algorithms Gradient-based algorithms are deterministic algorithms that optimize a problem by calculating the gradient of a differentiable function at a candidate $x^{(\text{k})}$ and then taking a step in the opposite direction of the gradient to calculate a new candidate $x^{(\text{k+1})}$ before repeating this procedure. The optimization will be complete, once either the function tolerance or the step tolerance threshold is crossed. While gradient-based algorithms are generally much faster than non-gradient-based algorithms, they are very sensitive to the initial value of the design variable in non-convex response spaces ending in a local minimum instead of finding the global minimum. In this work, the function `curve_fit` from the `Optim` package [43] and the function `nlsolve` from the

NLSolve package [43] for the Julia programming language [44] have been used as gradient based optimization algorithms.

Non-gradient-based Algorithms Non-gradient-based algorithms are stochastic algorithms that pursue variable (evolutionary) strategies to optimize a given problem. Since in this work only the metaheuristic-population-based genetic algorithm and particle swarm optimization solvers have been used, the following paragraph will only focus on giving a brief introduction to the fundamental idea of said algorithms. A detailed overview of other non-gradient-based algorithms can be reviewed [40].

Genetic algorithms are based on Darwin's theory of evolution. For the optimization of a given problem, the fitness of a randomized initial population within the feasible domain is tested. With respect to the fitness of each candidate, new generations are derived until a stopping criteria is reached. [40]. The initialization of a new generation is subject to randomized crossovers and mutation statement, which follows the idea of the Darwinian theory and is a statistical process [45]. The function ga from the Evolutionary package [46] was used for the implementation in julia

Another solution approach are particle optimization algorithms. Similar to the the genetic algorithms, an initial randomized population is distributed in the feasible domain. However, each initial particle is given a weight and an initial velocity, with which the particle moves in the feasible domain. For each iteration, the current fitness is tested at the current position and a new position is calculated which is determined from the inertia of the particle, the social weight and the cognitive weight. The cognitive weight induces a change towards the direction of the position with the best fitness that the individual particle has found. The social weight induces a change towards the direction of the position with the best fitness that the swarm has found. These changes act against the inertia which lets the particle travel on the previously designated path [47]. Hence, each particle's velocity in space is updated to is designated path, the particle's best position and the social best position of the swarm. The change of direction is further multiplied with a randomized acceleration constant [45]. This algorithm can be implemented with the *Manopt* package in Julia [48] or the Optim package [43]. The function particleswarm from the Optim package [43] was used for the implementation in Julia .

3 Literature Review

A photocatalytic reactor is used in the FlowPhotoChem project to reduce carbon dioxide to carbon monoxide using the reverse water gas shift reaction. The theory of photocatalysis was introduced in chapter 2.2.4. The mechanism is widely used throughout various industries such as waste water treatment, hydrogen production and purification of air [49].

$$CO + H_2O \rightleftharpoons CO_2 + H_2 \tag{R9}$$

However, throughout this work legitimate doubt on the photo catalyst reaction mechanism emerged. In most studies, the detection of product is often considered as proof for a successful photocatalytic conversion. However, studies performed with isotope labeling and untreated as photocatalyst demonstrated the insufficiency of this proof for CO [50] and CH_4 [51], since these products have been found with the isotope labeling to result from carbon residues in the reactor and not from the gas feed. Therefore, results mus be treated with great caution and product formation distributions can be distorted from contamination. A multitude of studies for different reverse water gas shift catalysts have been published [52–59], but significant less for photocatalytic reverse water gas shift reactions [60]. Photocatalytic systems in general and unspecific towards the product, have been evaluated and compared in the work of Habisreutinger et al. [36]. Table 3.1 shows the distribution of photocatalytic systems for different products. With less than 11 % for photocatalysts on titanium basis, the reduction mechanism remains not very well understood [36].

3.1 Comparison Photochemical Versus Photothermal

During the simulation process, experimental data for the inlet and the outlet temperature has been requested from external project partners in Valencia for the validation of the thermal modeling of the photocatalytic reactor. In an E-Mail correspondence, it has become

Table 3.1: Overview of photocatalytic systems.

	TiO_2 Basis		no TiO_2	
CO	5	10.9%	9	18.8%
CH_3OH	9	19.6%	7	14.6%
CH_4	23	50.0%	16	33.3%
HCOOH	2	4.3%	13	27.1%
$CH_4 + CH_3OH$	1	2.2%	-	-
CH_4N_2O	1	2.2%	-	-
$HCOOCH_3$	1	2.2%	-	-
$HCOO^-$	1	2.2%	-	-
$CH_4 + C_2H_4$	3	6.5%	-	-
HCHO	-	-	1	2.1%
C_2H_5OH	-	-	1	2.1%
oxalate	-	-	1	2.1%
	46	100.0%	48	100.0%

apparent that at a artificial irradiation of 50 suns, the temperature inside the reactor reaches 550 °C-500 °C in the latest experimental set-up, but in other circumstances temperatures of 700 °C-750 °C have been recorded. Additionally, for one of the two experimental set-ups from the external partners, the reactor only produced the desired product when the feed stream was preheated to temperatures of approximately 100 °C. For temperatures greater than 800 °C, the reverse water gas shift reaction becomes thermodynamically favorable. The temperature was calculated using the Nasa7 polynomials for the heat capacity c_p, the entropy S, and the enthaply H and the corresponding NASA7 polynomial fits openly accessible from the Gri-Mech 3.0 mechanism [18]. The parameters can be seen in Source Code B.2.

$$C_p = (a_1 + a_2T + a_3T^2 + a_4T^3 + a_5T^4)R \tag{3.1}$$

$$H = RT(a_1 + (a_2T)/2 + (a_3T^2)/3 + (a_4T^3)/4 + (a_5T^4)/5 + a_6/T) \tag{3.2}$$

$$S = R(a_1 log(T) + a_2T + (a_3T^2)/2 + (a_4T^3)/3 + (a_5T^4)/4 + a_7) \tag{3.3}$$

and the change of the Gibbs free energy ΔG_{Rxn} for the reaction.

$$\Delta G_{Rxn} = \Delta H_{Rxn} - T\Delta S_{Rxn} \tag{3.4}$$

The results are shown in figure 3.1 show the Free Gibbs Energy and the equilibrium constant as function of the temperature. The calculations have been validated against

previous work from [61].

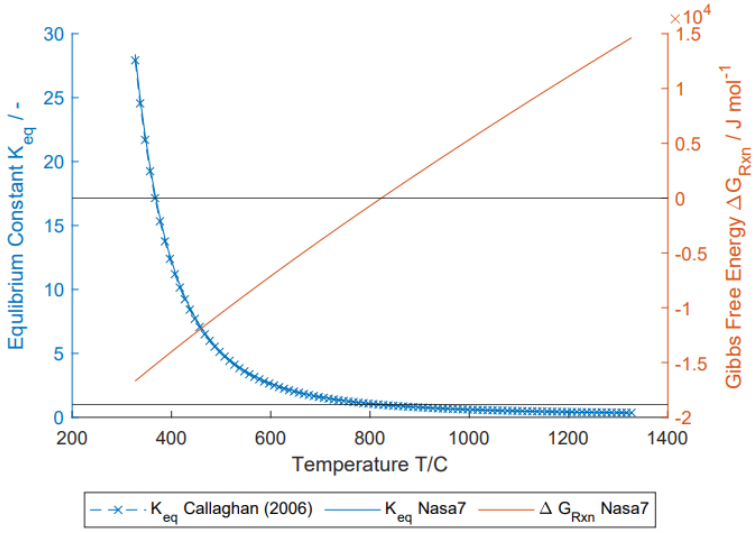

Figure 3.1: Temperature dependency for the thermodynamic equilibrium and Gibbs free energy for the water gas shift reaction.

As a result of these calculations, part of this work focused on finding literature, that clarifies, weather the process was mainly driven by a photo-thermal or a photo-catalytic reaction mechanism. Dubi et al. [62] evaluated the reaction rates as a function of light intensity, wave length and temperature and concluded that the reaction mechanism is solely photo-driven. If the reactor temperature is evaluated accurately, the reaction rates in all papers reviewed follow Arrhenius theory.

3.2 Simulation Methodology

One core component of the work in the FlowPhotoChem project is to find simplified models for each of the three reactor types used that are suitable for the process simulation software. Significant progress has been achieved in previous work for the process simulation of the electochemical reactor modules. For the photo-catalytic reactor questiosn the question of a suitable reactor model and reaction kinetic was unsolved. A thorough literature review on a reactor simulation model with of a photocatalytic reverse water gas shift reaction rate did not result in satisfactory solution. In the following, the most

promising publications will be briefly introduced.

Xu and Froment [63, 64] reported intrinsic reaction rates for the thermal reverse water gas shift reaction using a $Ni/MgAl_{204}$ catalyst. The paper has not only become a common used basis for steam reforming, but also provides an intrinsic reaction kinetic for the reverse direction. Vidal-Vazquez[65] deduced a reduced reaction rate at high temperatures and pressure based on the results of Xu and Froment. Bustamente et al. simulated an uncatalyzed homogeneous quartz reactor at a pressure of 1 bar and temperatures between 1148 K and 1198 K using a power-law rate expression. Kim et al. [66] states a reaction rate for the reverse water gas shift reaction with a Pt/TiO_2 catalyst. Upadhye et al. [60] deduced a plasmon-enhanced reaction rate for the reverse water gas shift reaction. Zhang et al. [67] simulated his a packed bed reactor for the water gas shift reaction with the minimization of the entropy. And Hernandez Lalinde et al. [68] and Daza et al. [55] provide a tabular overview of different reaction rates and discuss the assumptions and catalysts used.

4 Modeling and Implementation

Three reactor concepts are utilized in the FlowPhotoChem Project, two Photo-Electrochemical (PEC) reactors, the Photo-Electrochemical Proton Exchange Membrane Water Electrolyser (PEC-PEMWE) ractor and the Photo-Electrochemical Carbon Dioxide Reduction (PEC-CO2R) reactor, one Electrochemical (EC) reactor, the Electrochemical Carbon Monoxide Reduction (EC-COR) reactor, and one Photo-driven, possibly Photocatalytic (PC) reactor for the reduction of carbon dioxide thorugh the reverse water gas shift reaction. Although the nature of the working principle of the PC reactor is not fully understood at this point, which might either be photocatalytic or photothermal, as has been discussed in the literature review (see chapter 3), the internal designation for the reactor is photocatalytic reactor and hence throughout this work, the name will be used accordingly.

Each reactor model uses different structures, variables and port types that need to be imported into Aspen Custom Modeler® in the correct order. To simplify this procedure, a user defined library has been created that loads the models in the correct order. The directory structure can be seen in figure 4.1. Its library includes the default Aspen Custom Modeler® library and the dynamics library that come preinstalled with Aspen Custom Modeler® . All models from previous work in the project are included in the library together with newly created models that can be identified by the short description on the right of the directory tree. Since progress has been made simultaneously, some structures and models can and should be unified in later stages in the project such as, e.g. *MainProps* and *MyProps*.

In the following chapters, each reactor model used in the process simulation will be introduced. Each chapter describing one reactor or component model will follow a common certain structure. Firstly, the geometry and the designing parameters will be given. Secondly, the model choice and level of detail, its implementation and model parameters will be listed. Lastly, depending if experimental data was available or found in the reviewed literature, either a model verification or validation according to the definitions given by the

American Institute of Aeronautics and Astronautics [69] will be discussed. Verification is defined as :

> "*the process of determining that a model implementation accurately represents the developer's conceptual description of the model and the solution to the model.*" [69].

Validation is defined as :

> "*the process of determining the degree to which a model is an accurate representation of the real world from the perspective of the intended uses of the model*" [69].

- /FlowPhotoChem
  - Dynamics — Aspen Custom Modeler® library with Aspen Plus® models and submodels
  - Modeler — Generic Aspen Custom Modeler® Library
  - Models
    - ECCO2R_Electrolyser — CO_2 electrolyser with η_{act} and η_{ohmic} losses
    - ECCOR_Electrolyser — CO electrolyser with η_{act} and η_{ohmic} losses
    - Holdup
    - PBR
    - PEMWE
    - PEMWE_Electrolyser — H_2O electrolyser with η_{act} and η_{ohmic} losses
    - PEMWE_Performance
    - PEMWE2
    - PhotoThermalS3P
    - PV_noCooling — GaInP/GaInAs/Ge triple junction concentrated PV cell w/o cooling
    - React
    - Tank
    - TripleJunctionPV — GaInP/GaInAs/Ge triple junction concentrated PV cell
  - ParameterTypes
    - MembraneThickness
  - Port Types
    - MassOnly
    - ElectricalPort — Port for voltage, current
  - Stream Types
    - MassStream
    - Electrical — Voltage, current Stream with efficiency
  - Structure Types
    - ECCOR — Phenomenological CO clectrolyser reaction structure for half cell reaction
    - MainProps
    - MyProps — User defined constants
    - PEC_Electrolyser_Pheno — Phenomenological CO_2 electrolyser reaction structure for half cell reaction
    - PEMWE_Electrolyser_Pheno — Phenomenological CO_2 electrolyser reaction structure for half cell reaction
    - PhotoThermal
    - PhotoThermalRuSTO
    - PhysConst
    - Reaction
    - WaterSplitting
    - WaterSplittingHalfCells
  - Variable Types
    - resistance — Electrical resistance with upper and lower limits

Figure 4.1: Directory tree for the FlowPhotoChem library in Aspen Custom Modeler® .

4.1 Photovoltaic Module

In this work, solar energy is both used as photo-thermal and electrical energy source for different reactor concepts. For the latter, a GaInP/GaInAs/Ge triple junction concentrated photovoltaic module was used in the experimental work from external project partners to operate the electrolysis. The implementation follows the theory explained in chapter 2.2.1. The parameters for the PV module implemented in this work have been obtained from Segev et al. [26] complemented with data from Holmes-Gentle et al. [30]. In this work, the PV model was implemented in Aspen Custom Modeler® following the implementation in Julia from previous work in the FlowPhotoChem project. Table A.1 summarizes the relevant modeling parameter from Segev et al. [26] and Holmes-Gentle et al. [30] necessary for the implementation. The PV model in Aspen Custom Modeler® has one electrical port with a minimum number of connections of one. The model is underspecified by one variable and either the current or the voltage of the electrical stream should be fixed to have equally many calculated variables as equations, if no electrical consumer unit is connected to the photovoltaic model with an electrical stream.

During the preparation of this thesis but after the access to the simulation program and the data has expired, it was discovered that the molar production rate and the energy equations of the PV model in Aspen Custom Modeler® falsely only considers the area of a single cell instead of the are of the module. Thus, both equations must be updated and the number of serially and parallel cells in the PV module must be factored into the equations. Furthermore, the power of the single PV cell is calculated correctly, but was not adapted to match the displayed unit in the output table. The table uses kW as display unit, while the calculation uses W for electrical power.

Validation The implemented model has been tested against the current-voltage characteristic curves for different solar irradiation presented in Holmes-Gentle et al. [30]. Interim and output port variables were compared to the model implemented in Julia from previous work in this project. The wrong calculations of the power and the area possibly resulted from working with an outdated model since at the time, the validation was successful. The model should be reevaluated and the validation procedure repeated.

4.2 Electrolyser Module

The thermodynamic fundamentals that form the basis of electrolyser modeling are discussed in chapter 2.2.2. This work includes the implementation of three types of electrolysers modules throughout the process variants, namely the photo-electrochemical proton exchange membrane water electrolyser (PEC-PWEMWE), the electrochemical carbon monoxide reduction reactor (EC-COR) and the photo-electrochemical Carbon Dioxide (PEC-CO2R) reactor. In this chapter, the generic details of the implementation of the electrolyser model that are common for all three electrolysers will be discussed firstly. Secondly, the specific details for each of the three electrolysers will be described in the following subchapters.

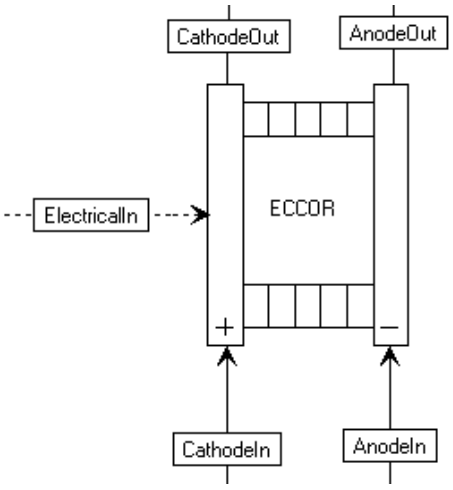

Figure 4.2: Aspen Custom Modeler® block representation of an electrolyser model.

Figure 4.2 shows an electrolyser block implemented in Aspen Custom Modeler® and the port connections to the block. The model requires one electrical stream input connected to an electrical port. If the electrical port is not connected, the setup of the flowsheet is displayed in the simulation software Aspen Custom Modeler® as incomplete. The user is informed in the specification statues evaluation to connect an electrical input stream. Furthermore, four material ports, corresponding to two input and two output streams can be connected to the model. The minimum number of streams required for each port is set to zero and the flow rate of the inlets are set to the component net formation rate resulting from the applied electrical current. The inlet port variables describing the stream composition in case of reverse flow through the electrolyser block are set to the corresponding values calculated for the stream composition connected to the corresponding outlet to assure the self initialization and provide the correct values where the flow direction could reverse according to changing pressure levels in the inlet and outlet. This allows for an easy use in pressure driven simulations. It was found to improve numerical stability when a reduced component list that includes only the minimum number of components required for the reaction. Otherwise, the vapour-liquid-equilibrium (VLE) calculation often failed to solve if components in the stream were present at a mole fraction near zero. Although not advisable, the model self initializes the component lists and can perform with any component list specified in the model and without the

necessity to adapt the equation sets in the model. By default, the model is underspecified by one degree of freedom and either the current or voltage input in the electrical stream or the total current density in the electrolyser block should be fixed to fully specify the simulation. If the electrolyser block is directly connected to the photovoltaic block, the model is fully specified and the intersection of both current-voltage curves determines the operating point of both the electrolyser and the PV module. Furthermore, the anode and cathode streams are assumed to be in thermal equilibrium and their common temperature is obtained from an energy balance around the electrolyser. Pressure losses are implemented in the model but are currently set to zero. They can be included for both cathode and anode by changing the default value to an experimentally determined value.

The operating voltage of an electrolyser is given by equation 2.40, which is a sum of the reversible voltage required for the electrochemical reaction and three loss terms described in detail in the theory chapter 2.2.2. To derive an electrolyser mode fully dependent on operating temperature and pressure, each contribution in equation 2.40 must be expressed as a function of the parameters. The following paragraphs will discuss the modeling approach of each contribution. In case of a single electrochemical reaction such as in the PEC-PEMWE, the equivalent net formation rate can be calculated from Faraday's second law of electrolysis 2.37. If more than one oxidation reactions occurs in an electrolyser, e.g. in the EC-COR and PEC-CO2R reactor, byproducts are formed and each half cell reaction must be included in the modeling approach.

Reversible Voltages The reversible voltages an be calculated from the Gibbs free energy change associated with the reaction. The values for the Gibbs free energy can be obtained by calling physical property functions in the reactor models that access Aspen's built-in property database. However, it was found, that the reversible voltages calculated from the Gibbs free energy change of the reaction did not match the voltages in the literature. Once the problem was systematically analyzed, the error could be related to the Gibbs free energy of formation at 25 °C of the hydroxide ion obtained from the property call. The output of the Aspen property call in Aspen Custom Modeler® was −137.1 kJ/mol. Calculation in this work resulted in −157.3 kJ/mol. This value was later validated with a given value of −157.2 kJ/mol in Bui et al. [70]. Since this value is calculated at standard temperature and pressure (STP) conditions, the Gibbs free energy, the enthalpy and the entropy must be corrected to non standard temperature and pressure using equation 2.6 for the enthalpy and equation 2.7 for the entropy. Since the implementation of these thermodynamic relations would be rather time expensive to implement, the support

center should be contacted first to possibly resolve the property call issue. If one were to implement these relations, the implementation could be achieved with the polynomial approximations of thermodynamic properties such as the NASA7 or Shoemate polynomials. Since the validity of the Gibbs free energy value for the hydroxide ion was unclear before it was possible to confirm with literature, the reversible voltages of each half cell reaction in the current state of the models is implemented as fixed value. Therefore, the reversible voltage is not yet dependent on temperature and pressure. However, the user can adapt the model of the electrolyser from a fixed reversible voltage to a calculated reversible voltage for the half cell reaction by changing *E_rev* to *E_rev_calc* in the *Output Voltage* section of the Electrolyser model (see Source Code 4.1). However, it should be noted, that if this adaptation is made, all other contributions to the cell voltage must also be dependent on the operating temperature and pressure. As described in the following paragraphs, the activation overpotential of the electrolyser does not depend on the operating temperature and pressure since the model fit was unsuccessful. Thus, the current model derives a fixed reversible voltage at STP for the half cell reactions.

Source Code 4.1: Code section for the output voltage of the electrolyser model in Aspen Custom Modeler® .

```
//_____________________________________
// OUTPUT VOLTAGE
//_____________________________________

        /*
        Closure Realations between Cathode and Annode.
             - Each Half Cell reaction needs to be at the same
                 Voltage (parallel coupled Reactions)
             - current density fluxes for Cathode and Anode
                need to be equal
        */
        SIGMA(j_cell(IRxn.RxnSetsCathode)) = j_cell_tot;
        j_cell_tot = SIGMA(j_cell(IRxn.RxnSetsAnode));
        For Set in IRxn.RxnSetsAnode DO
            E_an = IRxn.E_rev(Set) + eta_act(Set);
        EndFor
        For Set in IRxn.RxnSetsCathode DO
            E_cat = IRxn.E_rev(Set) + eta_act(Set);
        EndFor
```

If multiple reactions occur in parallel at an electrode, which is the case if byproducts are formed, each reaction must satisfy two fundamental criteria. Firstly, the total voltage of each half cell reaction must be equally large since each electrochemical reaction constitutes a thermodynamic barrier and thus, can be concluded as a parallel circuit resistance.

Secondly, the total electrical current density in both half cells must be equally large since each half cell reaction of the redox reaction due to charge conservation. Therefore, the half cell reaction rates can be concluded as series circuit of resistances.

$$V_{\text{cat}} = E_{\text{i, cathode half cell rxn}} + \eta_{\text{act,i, cathode half cell rx}} \tag{4.1}$$

$$V_{\text{an}} = E_{\text{k, anode half cell rxn}} + \eta_{\text{act,k, anode half cell rxn}} \tag{4.2}$$

$$j_{\text{total}} = \sum_{l} j_{\text{l, cathode half cell rxn}} = \sum_{m} = j_{\text{l, anode half cell rxn}} \tag{4.3}$$

Activation Overpotential Losses In the current state of the carbon monoxide and carbon dioxide reduction electrolyser models, the activation overpotential loss contribution is fitted to a Tafel kinetic. The phenomenological model includes an additional linear contribution. The piecewise model also includes a linear contribution in low current density regions an additional quadratic contribution above a threshold value for the current density j_{L} (see equation (4.4)). The first will be denoted as phenomenological model and the second as piecewise fit. Both models account for deviations from the logarithmic nature of the tafel kinetics in higher current density regions. Arguably, the observed deviations from logarithmic relationship addressed by the model extensions could be caused by a mass transport related overpotential. The choice to account for both overpotential contributions cumulatively was made during earlier work in this project and is listed here for reasons of completeness.

$$\eta_{\text{act/mtx}} = \begin{cases} b \log_{10}\left(\frac{j}{j_0}\right) + j\,\Omega, & j \leq j_{\text{L}} \\ b \log_{10}\left(\frac{j_L}{j_0}\right) + j_{\text{L}}\,\Omega + (j - j_{\text{L}})^2\,\Omega^* & j > j_{\text{L}} \end{cases} \tag{4.4}$$

with the optimization parameters b, j_0, Ω, j_{L}, and Ω^*.

In this work, it was tried to develop a modeling approach that would allow the separate calculation of activation and mass transfer overpotential providing two advantages. Firstly, the linear and quadratic contributions in the phenomenological and piecewise function do not satisfy the equation (2.47). When using the model in its current form, applying larger external voltages causes larger reaction rates. However, if the maximum diffusion mole flux though the boundary layer of the fluid-solid interface is reached, the maximum reaction rate is also limited to the mole flux from diffusive material transport. Therefore, the phenomenological and piecewise models are not valid for current densities that exceed the experimental data that their parameters were fitted on. This work addressed

this problem by using equations for the activation and concentration overpotentialy that satisfy the requirements in (2.47). Secondly, the Tafel kinetic in the form $b\log(j/j_0)$ does not include a dependence on temperature. Therefore, a temperature dependent activation overpotential (4.5) from Fuel cell literature [8] was used. The results of this parameter fit will be discussed in detail in chapter 5. Since the model fit was inconclusive, which also will be discussed accordingly, the current electrolyser models are implemented using the equation set 4.4 and the model should be retested if more experiential data for different temperatures and a broader range of voltage and current density measurements become available. In the temperature dependent activation overpotential is α the charge transfer coefficient, j_0 the exchange current density, and E_A the activation Energy.

$$\eta_\mathrm{act} = \frac{RT}{\alpha z_\mathrm{e} F} ln\left(\frac{j}{j_0 \exp\left(-\frac{E_\mathrm{A}}{RT}\right)}\right) \tag{4.5}$$

Regarding the model implementation in Aspen Custom Modeler® the parameter set for the activation overpotential calculation is specified in the reaction structure of the model. If the current density threshold value j_L is exceeded, the electrolyser model switches from the phenomenological model to the piecewise model. The Source Code 4.2 shows the various contributions of the model to the activation overpotential. If the phenomenological model is to be used only, one can specify a very high value in the reaction structure for the limiting current density to deactivate the piecewise function (see line 7 in Source Code 4.2).

Source Code 4.2: Phenomenological and piecewise implementation for the activation overpotential used in electrolyser models in Aspen Custom Modeler® .

```
1  //_____________________________________
2  // ACTIVATION LOSSES
3  // Tafel Equation
4  //_____________________________________
5
6  For Set In IRxn.RxnSetsAll Do //RxnSetsAll
7  If j_cell(Set) < IRxn.ParameterPhenomenological(Set,"p4") THEN
8    // Phenomenological Model
9     ActivationLosses: eta_act(Set) =
10         //Regular Tafel Equation Contribution
11                 IRxn.ParameterPhenomenological(Set,"p1") *
                      LOG10(j_cell(Set) / IRxn.
                      ParameterPhenomenological(Set,"p2"))
12         // Linear Contribution to better fit the Measured Data
               (Boutin 2022 und Endrodi 2020, and 2021
13           + IRxn.ParameterPhenomenological(Set,"p3") * j_cell(
                Set);
```

```
Else                                                                    14
  // Piecewise Function                                                 15
   ActivationLosses: eta_act(Set) =                                     16
        //Regular Tafel Equation Contribution                           17
                IRxn.ParameterPhenomenological(Set,"p1") *              18
                   LOG10(j_cell(Set) / IRxn.
                   ParameterPhenomenological(Set,"p2"))
        // Linear Contribution to better fit the Measured Data         19
            (Boutin 2022 und Endrodi 2020, and 2021
          + IRxn.ParameterPhenomenological(Set,"p3") * IRxn.            20
             ParameterPhenomenological(Set,"p4")
        // Non-Linear Contribution from Piecewise fit                   21
          + (j_cell(Set)-IRxn.ParameterPhenomenological(Set,"           22
             p4"))^2*IRxn.ParameterPhenomenological(Set,"p5");
ENDIF                                                                   23
EndFor                                                                  24
```

Concentration Overpotential Currently, the concentration overpotential is not explicitly considered in the electrolyser model as independent equation, but rather in a unified approach for activation and concentration overpotential using one equation. The contribution can be included using equation (2.40). The equation is dependent on the temperature of the reactor and the limiting current density which needs to be determined. This can either be done analogous to the activation overpotential via parameter fitting, if experimental data becomes available for higher current densities or analytically. For the latter approach the diffusion mass flux from the bulk gas phase to the surface of the electrode is solved numerically. The diffusion coefficient calculation for the gas phase and all relevant parameters are referenced and included in the diffusion theory chapter 2.1.2 of this work. The effective diffusion coefficient in porous media can be calculated from the free space diffusion coefficient corrected by the tortuosity and porosity of the porous gas diffusion layer. The mole flux resulting from the solution of the diffusion problem can be used to solve the corresponding current density using Faraday's law of electrolysis to determine the limiting current density.

4.2.1 Anode

The anode half cell reaction is identical for both carbon monoxide and carbon dioxide reduction electrolyser models used in this work and therefore will be introduced beforehand. The electrolyser half cell is solely composed of the oxygen evolution reaction (R10) in

an alkaline environment (pH=14). The reversible voltage is measured against the Normal Hydrogen Electrode NHE.

$$4\,OH^- \longrightarrow 2\,H_2O + O_2 + 4\,e^- \qquad E^0_{redox} = 0.401V \qquad \text{(R10)}$$

The extended Tafel kinetic model (phenomenological model) in equation (4.4) was fitted to experimental data from Endrődi et al. [71] previously. For reasons of completeness the parameter set for the phenomenological modeling approach with three parameters used in the model is included in this work, but since it was not part of this work it will not be discussed in detail.

$$b = 0.0426207 \tag{4.6}$$
$$j_0 = 7.90112 \cdot 10^{-12} \tag{4.7}$$
$$\Omega = 0.120405 \tag{4.8}$$

4.2.2 Verification

Each electrolyser consist of the reaction structure and the base model of the electrolyser. For the verification of the generic part of the electrolyser base model, the overall and component mass balances have been checked. Furthermore, voltages and current characteristics have been reviewed against the experimental data used in previous work for the ECCOR reactor and for the PEC-CO2R reactor as part of this work.

4.3 Photo-Electrochemical Reactor

Conceptually, the Photo-Electrochemical (PEC) reactor denotes a thermally and electrically integrated electrolyser and photovoltaic module. In this work, two PEC reactor variants have been considered in the process simulation. The coupled proton exchange membrane water electrolyser (PEC-PEMWE) reactor PEC-PEMWE produces hydrogen from water splitting that will be used downstream for the production of carbon monoxide from water gas shift reaction in the photocatalytic (PC) reactor. The electrochemical carbon dioxide reduction reactor PEC-CO2R is used as an alternative concept for the PEC-PEMWE and PC reactor to directly produce CO from electrochemically reducing

CO_2. Both PEC reactors will be introduced in the following chapters.

4.3.1 Photo-Electrochemical Carbon Dioxide Reduction Reactor

The reactor model is based on coupling the electrolyser and photovoltaic models discussed in the previous chapters. The anode water flow is also used for the cooling of the photovoltaic cell energetically coupling the two components. The anode half cell reaction is the oxygen evolution reaction (R10). The cathode half cell reactions and the corresponding modeling approach is described in the following section.

Cathode Activation Overpotential The cathode overall and the two half cell reactions for carbon dioxide reduction electrolyser are given in reaction (R11)-(R13). The reversible voltages were measured against the reversible hydrogen electrode (RHE) [72]. The carbon dioxide reduction half reaction is desired for the production of carbon monoxide. The water half cell reaction is an undesirable side reaction with hydrogen as byproduct.

$$\mathrm{CO_2} \longleftrightarrow \mathrm{CO} + \frac{1}{2}\mathrm{O_2} \qquad \frac{\Delta G^0}{2F} = 1.33V \qquad \text{(R11)}$$

$$\mathrm{CO_2} + 2\mathrm{e^-} + 2\mathrm{H^+} \longleftrightarrow \mathrm{CO} + \mathrm{H_2O} \qquad E^0_{\mathrm{redox}} = -0.1V \qquad \text{(R12)}$$

$$\mathrm{H_2O} \longleftrightarrow \frac{1}{2}\mathrm{O_2} + 2\mathrm{e^-} + 2\mathrm{H^+} \qquad E^0_{\mathrm{redox}} = 1.23V \qquad \text{(R13)}$$

Figure 4.3 shows the experimental partial current densities from Boutin et al. [72] that were used to fit the cathode activation overpotential. The reversible potentials of the cathode half cell reactions were calculated using equation (4.10). The anode activation overpotential was available from previous work. The ohmic overpotential was determined from the electrochemical impedance spectroscopy measurement from Boutin et al. [72]. Since the reported experimental data composed of only three measurements at different voltages, the fitting parameters of the model was challenging and is reliant on subjective consideration of the results. Figure 4.4 shows an fairly easy distinction between an unsuccessful and a successful parameter fit. However, due to the limited size of the experimental data and additionally for the partial current density of hydrogen the narrow range in which experimental data was obtained different parameter fits can be obtained that visually appear equally well fit. Thus, the selection of the best parameter fit is subjective and the parameter fit procedure should be repeated once more data becomes available. The datasets include for neither carbon monoxide nor hydrogen experimental data in lower and higher current density regions. For hydrogen, only low partial current densities and for carbon monoxide production only high partial current densities are reported. This will impact the validity of the parameter fit in the regimes of partial current densities with no experimental measurements reported.

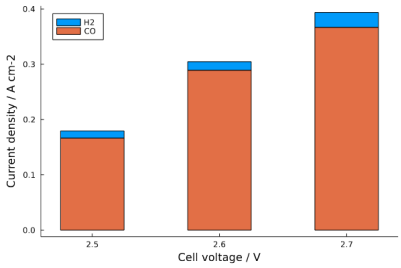

Figure 4.3: Experimental data from Boutin et al. [72] for the partial current densities of the CO and H_2 cathode half cell reactions of the PEC-CO2R reactor.

$$U_{\text{cell}} = E_{\text{rev}} + \eta_{\text{act/conc}} + \eta_{\text{ohmic}} \tag{4.9}$$

$$= (E_{\text{rev, an}} + E_{\text{rev, cat}}) + (\eta_{\text{act/conc, an}} + \eta_{\text{act/conc, cat}}) + \eta_{\text{ohmic}} \tag{4.10}$$

The phenomenological and piecewise model parameters were fitted to the experimental data. The phenomenological model showed good agreement with the experimental data. However, it must be noted, that best fit for the function with wide bounds was overfitting the model to the data, since the model has equally number of parameters as number of experimental responses. Therefore, for many data sets the problem can be solved algebraically such that the model maps each experiential point exactly. While the experimental response are certainly mapped very accurately, yet the model does not depict a valid physically basis which is a common result of overfitting. A set of very large parameters must be used to map the experimental data exactly. Therefore, the bounds for the optimization algorithm were tightened to find a physically valid model fit. Table 4.1 shows the optimization parameters for the successful and for the unsuccessful model fit. Figure

4.4 shows the results of the successful and unsuccessful fit of the phenomenological model and the results of the piecewise model fit. The phenomenological model was chosen for the implementation in Aspen Custom Modeler® since the model was most consistent with the experimental data.

Table 4.1: Optimization parameter sets for the electrolyser overpotential parameter fit. For reasons of comprehensiveness, the reader is encouraged to check the nomenclature for units.

Optimization set	Lower Bound	Upper Bound	Starting Value
unsuccessful	b=-10 p_2=10^{-15} p_3=-100	b=50 p_2=500 p_3=100	b=1 p_2=10^{-2} p_3=10
successful	b=1 p_2=10^{-2} p_3=0	b=50 p_2=50 p_3=10	b=1 p_2=10^{-2} p_3=10

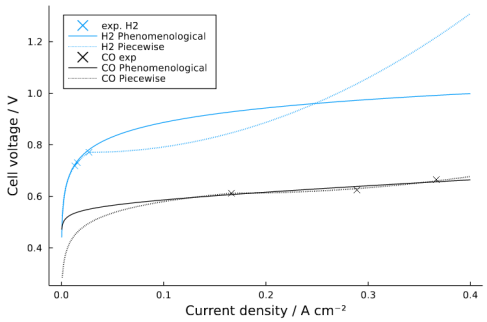

(a) Results of the piecewise and phenomenological activation overpotential parameter fit.

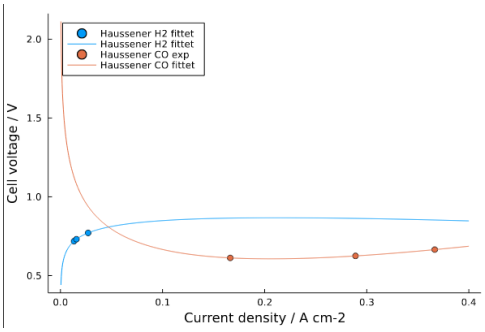

(b) Overfitting result of the temperature dependent activation overpotential fitting model.

Figure 4.4: Cathode activation overpotentials parameter fit for the PEC-CO2R reactor.

Table 4.2 shows the parameters for the activation overpotential for the cathode half cell reactions for the phenomenological model and for the temperature dependent model. The data set used for the parameter fit for a single temperature and at different voltages. Therefore, both parameter sets are only valid for a fixed temperature. When the activation overpotential fit for different temperatures and voltages with experimental data from Endrődi et al. [73] and Boutin et al. [72] was performed the result was unsuccessful. This is considered in detail in the discussion chapter of this work.

Table 4.2: Parameters for the cathode half cell reaction overpotential.

Phenomenological model	b / V	j_0 / A/cm^2	Ω / Ωcm^2
η_{act} CO	0.612208	0.6248	0.664822
η_{act} H_2	0.718208	0.7308	0.770822
Temperature dependent model	α / -	j_0 / A/cm^2	E_A / J/mol
η_{act} CO	0.128223	1.2500810^{-6}	18.263
η_{act} H_2	0.0998811	2.8166710^{-7}	2.78536

4.3.2 Photo-Electrochemical Proton Exchange Membrane Water Electrolyser

The Photo-Electrochemical Proton Exchange Membrane Water Electrolyser (PEC-PEMWE) has already been investigated in great detail in the published literature [74] and thus, the electrolyser was implemented according to the theory chapter 2.2.2 utilizing model parameters obtained by parameter fit to experimental data from Suerman et al. [74] and work previously performed. The electricity needed for the electrolysis is provided by the triple-junction photovoltaic module. The water electrolyser model used throughout this work was previously and has not been updated to the model structure described in the chapters above. However, if desired the model can be adapted using the same model set up as described for the generic electrolyser reactor model implemented as part of this work. The model has neither been verified nor validated as it was taken from previous work.

4.4 Electrochemical Carbon Monoxide Reduction Reactor

The Electrochemical reactor module is used in the simulations for the reduction of CO_2 in the PEC-CO2R and CO in the EC-COR reactor. In difference to the PEC-CO2R, the ECCOR reactor is thermodynamically not coupled with a photovoltaic cell. The reactor parameters were taken from previous work in this project and the reactor module was unified with the generic electrolyser model implemented in this work. Thus, the details of the reactor are not discussed in this work, but Table A.2 shows all relevant parameters for the implementation. Further information in the reactor concept and experimental data can be found in Romero-Cuellar et al. [75].

4.5 Photocatalytic Reactor

During the duration of this thesis, an alternative flowsheet configuration for the production of carbon monoxide as intermediate product in the process has been adapted. While the initial design consisted of a PEC-PEMWE for the production of hydrogen and an PC reactor for the photocatalytic reduction of CO_2 to CO, in the alternative design these two have been substituted with a PEC-CO2R reactor after the methodology pivot. However, in interest of knowledge management, the current state of the model is preserved.

For the photocatalytic reactor, two design concepts have been developed. The first variant is denoted as the photocatalytic free stream reactor (PC(FSR)) and the second as photocatalytic packed bed reactor (PC(PBR)). Both reactor aim to photocatalytically convert carbon dioxide to carbon monoxide with the presence of a from solar irradiation photoexcited catalyst is present in the reactor. The focus switched from the first to the second variant during the duration of this thesis. The (PC(FSR)) modeling was initiated but not completed due to the decision to switch the design. The following chapter presents the progress achieved and the remaining steps to complete the PC(FSR) model with the inclusion of the reaction kinetics for the reverse-water gas shift (RWGS) and methanation reactions occurring in the PC reactor. In the following, both concepts will be introduced for completeness.

As result of the extensive literature review it was identified to the best of the authors knowledge that no photocatalytic reaction rate expression for the reverse water gas shift reaction suitable for the PC reactor model in this work has been fitted yet. From the literature review, the experiment available, and temperature measurements from the operation of the PC reactor it was derived, that the photocatalytic effect on the activity of the used catalyst for the reverse water gas shift reaction is negligible in respect to the the photothermal effect on the catalyst activity. This conclusion is based partly on the literature review, and partly on the missing CO yields for experiments at room temperature and under concentrated irradiation. For the production of CO to be detectable, temperatures of well above 100 °C were necessary in dark experiments. Although, this has not yet been ultimately confirmed, a parameter fit for the reaction rate equations from Vidal Vazquez et al. [65], which is an adapted kinetic model from Xu and Froment [63, 64] has been performed with a limited optimization parameter set. While only the literature review but not the parameter fit was part of this work and only the results have been used, the details of the kinetic model considerations are not included in this chapter.

4.5.1 Photocatalytic Free Stream Reactor

The initial design used for the photocatalytic reactor to reduce carbon dioxide to carbon monoxide via the reverse water gas shift reaction is had a disk shape with a diameter of 22 mm, a height of 2 mm with two pipes connected to the bottom of the disk. The inlet and outlet pipe with a diameter of 1 mm each are placed symmetrically at a distance of 1.5 mm from the outside of the disk edge to the center of the pipe. Figure 4.5 shows a cross section of the reactor along the x-z-plane.

The PC(FSR) model is based on the pseudo-homogeneous packed bed reactor reactor from Froment and Bischoff [76]. u_s is the space velocity, C_A the concentration of the component A, r the reaction rate per catalyst mass, ρ_B the catalysts density on the bed, z the space direction, ΔH_{rxn} the reaction enthalpy, U the heat transfer coefficientT_r the temperature of the reactor, d_p the diameter of the particle, and f the friction coefficient.

$$-\frac{\mathrm{d}(u_s C_A)}{\mathrm{d}} = r_A \rho_B \tag{4.11}$$

$$u_s \rho_B c_p \frac{\mathrm{d}T}{\mathrm{d}z} = -\Delta H_{rxn} r_A \rho_B - 4\frac{U}{d_t}(T - T_r) \tag{4.12}$$

$$-\frac{\mathrm{d}p}{\mathrm{d}z} = f\frac{\rho_g u_s^2}{d_p} \tag{4.13}$$

The model used in this work has three distinctions from the original model. Firstly, the pressure loss correlations for the porous media was removed. Secondly, the reaction rate was related to a catalyst mass on the surface (kg/m^2) instead of a reaction rate related to the catalyst mass in volume(kg/m^3). Thirdly, the cross sectional area along the space domain z in this work is not constant unlike in the original model. Therefore, the mean circumference of the disk was calculated and an equivalent hydraulic diameter was used in the model. The differential equations are implemented in Aspen Custom Modeler® using the partial differential equation toolbox and solved with a finite difference method solver.

4.5.1.1 Computational Fluid Dynamic Simulation

During the time of modeling, very limited experimental data has been available to validate the model implemented in Aspen Custom Modeler® . To gain a deeper understanding and to have an accurate 3D model representation of the reactor against which the 1D model can be compared to determine errors introduced by the various assumptions, a

computational fluid dynamics (CFD) simulation was set-up using the open source software OpenFOAM® .

Pre-Processing The reactor mesh was created with the previously introduced dimensions of the reactor volume. The inlet and outlet pipes were meshed with a length of 6 mm. The geometry can be seen in figure 4.5. Since the quality of the mesh is critical for a accurate CFD simulation result, the successful and unsuccessful meshing procedure is described in detail in the interest of knowledge conservation. Although unsuccessful in the end, the initial meshing approach using `snappyHexMesh` could almost be completed. Successfully meshing the geometry with `snappyHexMesh` provides a critical advantage in comparison to the currently used mesh since `snappyHexMesh` uses a structured grid that is iterative refined while the final mesh used in this work is an unstructured mesh. Structured meshes are highly space efficient and show an desirable high orthogonality. This reduces simulation time greatly and reduces numerical instabilities [77]. Since both phenomena were encountered in this work, the meshing procedure to the almost successful completion is described since a better mesh is advisable for future CFD simulations.

It was tried meshing with `snappyHexMesh` initially, with the geometry files created in the Open-

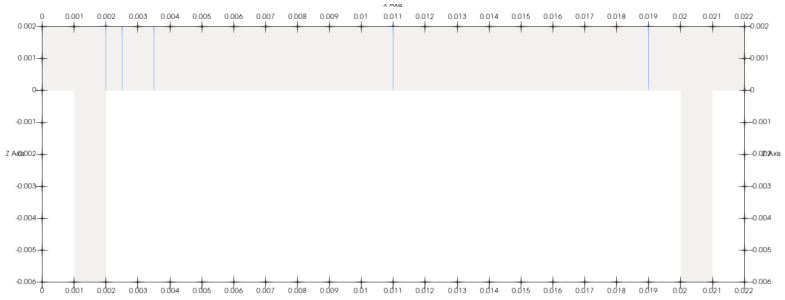

Figure 4.5: Cross section of the reactor volume geometry of the photocatalytic reactor on the x-z plane with the post processing probes included in blue.

Source software FreeCAD. The Geometry was exported as **.stl*-files. The `snappyHexMesh` algorithm was initialized with the parameter in table 4.3. The table only references the changes made in respect of the `snappyHexMesh` tutorial case. The edge Mesh files were created with the `surfaceFeatureExtract` utility.

However, it was found that the edges around the disk could not be resolved sharply and accurately. The results can be seen in figure 4.6. Increasing the minimum and maximum refinement levels in the castellated mesh control section or the level of refinement in the feature section of the **.eMesh*-file did not resolve the problem.

Table 4.3: Parameters for `snappyHexMesh` in OpenFOAM® .

Parameter	Value
Castellated Mesh Controls	
no changes	
Snap Controls	
no changes	
Add Layers Controls	
nSurfaceLayers	8
expansionRatio	1.1
finalLayerThickness	0.25
minThickness	1e-3
maxNonOrtho	65

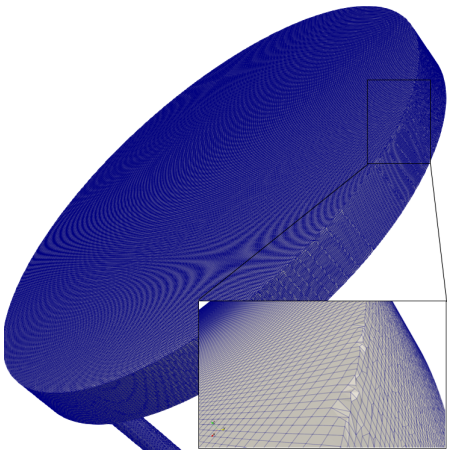

Figure 4.6: Results from the `snappyHexMesh` meshing.

Therefore, it was decided to create the mesh with an alternative software and convert the exported final mesh to the OpenFOAM® format. The mesh has been created with the NETGEN 1D-2D-3D algorithm in Salome v9. It was then exported as **.unv*-file and converted with `ideasToUnvFoam` and scaled from mm to m with the `transformPoints` utility. After the mesh had been converted, the patch types for all walls must be updated manually in the constant/polyMesh/boundary object from type *patch* to type *wall*.

In order to accurately resolve the subviscous boundary layers close the wall, two approaches can be taken. To fully resolve the boundary layers the first sublayer must be placed on the viscous sublayer at a dimensionless wall distance y^+-value of unity. Alternatively, the sublayers can be modelled with wall-functions that satisfy the physical constraints in the boundary layers. For this,

Table 4.4: Meshing Parameter for the NETGEN 1D-2D-3D algorithm for the mesh study.

Parameter	Coarse	Medium	Fine
Maximum size	0.5	0.3	0.1
Element size weight	0.05	0.03	0.01
Num. of surface optimization optimization steps	3	3	3
Num. of surface volume optimization steps	3	3	3

Table 4.5: Boundary layer meshing parameter used for the k-ω-SST-Model in OpenFOAM® .

Parameter	Value
Total thickness	0.2
Number of layers	8
Stretch factor	1
Extrusion method	surface offset + smooth

the y^+-value should satisfy the constraints in equation (4.14) [78, 79]. The meshing parameters for the coarse, medium and fine mesh of the mesh study can be seen in table 4.4.

$$30 < y^+ < 300 \tag{4.14}$$

The dimensionless wall distance y^+-value can be calculated with the following equations (4.15)-(4.18) [80] and a valid Reynolds and skin friction C_f correlation. In this case, the Prandtl's one-seventh-power law was used as correlation for local skin friction correlation (equation (4.15) [81]). τ_W is the wall shear stress, *rho* the density, u_∞ the free stream velocity, u_τ the friction velocity, $\hat{y}$ the absolute wall distance, and $y^+$the dimensionless wall distance, ν the kinematic viscosity.

$$C_\mathrm{f} = 0.0576 Re_\mathrm{x}^{-1/5} \qquad \text{for } 5 \cdot 10^5 < Re_\mathrm{x} < 10^7 \tag{4.15}$$

$$\tau_\mathrm{w} = \frac{1}{2} C_\mathrm{f} \rho u_\infty^2 \tag{4.16}$$

$$u_\tau = \sqrt{\frac{\tau_\mathrm{w}}{\rho}} \tag{4.17}$$

$$y = \frac{y^+ \nu}{u_\tau} \tag{4.18}$$

Considering that the first method requires substantial computational resources, the latter option was chosen. Since the geometry has a variable cross section area along the flow direction of the fluid, the wall distance for the boundary layer has been calculated such that the Reynolds number was calculated with the hydraulic diameter at the coordinate with the largest circumference ($x = 0.011mm$) and a y^+-value of 300. This assures, that the y^+-value for smaller circumferences is still greater than the lower bound of $y^+ = 30$.

The final unstructured mesh used for the simulations consists of a total of 1,675,392 prisms and 8,232,924 tetrahedron which add up to a total of 9,908,316 cells for the full geometry.

Few bad cells in the mesh, most likely the 20 cell faces with a small interpolation weight, were

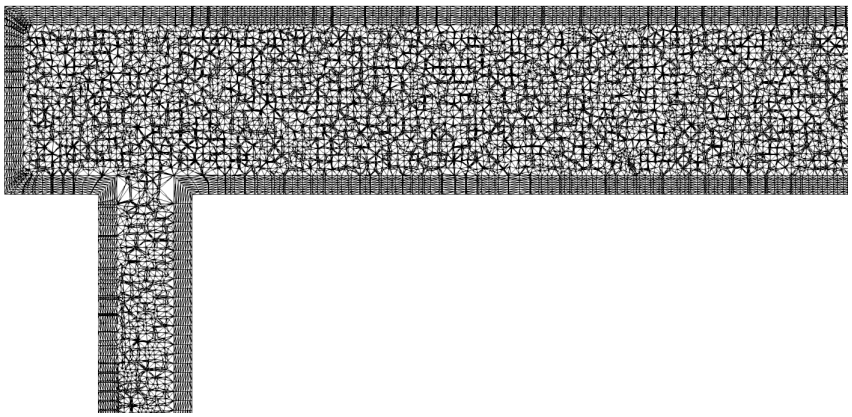

Figure 4.7: Cross section of the final mesh on the x-z-plane.

responsible for numerical stability problems for approximately the first 200 iterations causing the problem to diverge. This was especially critical for the `buoyantSimpleFoam` cases and could not be fully solved. But also for the `rhoSimpleFoam` cases, numerical instability occurred during the first iterations. This problem was solved for the laminar and turbulent cases with the `rhoSimpleFoam` solver and for the laminar cases with the `buoyantSimpleFoam` solver by including an options object in the case directory that limited the temperatures to a minimum of 200 °C and a maximum of 800 °C. After the first iterations and in the final results for the temperature field, these temperature bounds were not clipped in the domain. Furthermore, the temperature was initialized with the `setFields` utility. After the first iterations, the warnings from the temperature limiter did not occur anymore as the problem converged. Also, the initial 1000 iterations were run with the turbulence model deactivated, before it was reactivated to improve numerical stability. The turbulent `buoyantSimpleFoam` case did not converge successfully and further measures should be taken to improve the quality of the mesh.

The thermo-chemical properties were implemented using the `chemkinToFoam` utility and the Gri-Mech 3.0 files with the NASA7 polynomials for the enthalpy, entropy and heat capacity The transport properties were implemented with the Sutherland model. For the modeling of the turbulence, the SST $k-\omega$ model [82] was chosen, which combines the benefits of the standard $k-\varepsilon$ and the $k-\omega$ model and is generally a good choice for low Reynolds number simulations. Two equation eddy-viscosity models such as the SST $k-\omega$ model simulate the turbulence using the turbulence kinetic energy to account, specific dissipation rate and closure relations. The first quantifies the intensity of a turbulent flow and the second the dissipation rate of the turbulence kinetic energy. For laminar flow, the specific dissipation rate is much greater than the turbulent kinetic energy. Thus, even with an turbulence model present, the flow displays laminar behavior. Vice versa, without an turbulence model, the flow can only display laminar behavior. Although laminar flow was expected beforehand, the assumption should be checked. Thus, a turbulence model was chosen that performs well for low Reynolds number simulations to accurately detect possible turbulent behavior in the reactor.

Due to the very low free stream velocities in the reactor, the residuals satisfied the convergence criteria very rapidly. However, mass conservation was not satisfied as the outlet mass flux was still one order of magnitude smaller than the inlet mass flux. Hence, although the convergence criteria were reached, the simulation displayed no steady-state behavior. Therefore, the surface volume field ϕ has been logged with a function object and embedded in the control dictionary to check for steady-state conditions. The residual plot can bee seen in figure B.1.

Solver For the simulations, the two SIMPLE (Semi-Implicit Method for Pressure Linked Equations) solvers `rhoSimpleFoam` and `buoyantSimpleFoam` for compressible flow with heat transfer have been used to determine the flow characteristics and temperature distributions in the reactor. The differences between the two solvers become apparent from the OpenFOAM® header files for the pressure equation and the momentum energy equation. In contrast to the `rhoSimpleFoam` solver, `buoyantSimpleFoam` accounts for a radiation contribution in the energy equation and buoyancy contribution in the pressure equation. Because of numerical instabilities in the convergence of the `buoyantSimpleFoam` solver and since only the velocity and temperature profiles were of interest, the `rhoSimpleFoam` solver was chosen in this work and the temperature was fixed with a Dirichlet boundary condition to achieve first results in this work. To gain an deeper insight into the photocatalytic reactor concept further simulations could include radiation heat transfer, especially since there is in-house experience in the field of radiation simulation with the adapted `sfBuoyantSimpleFoam` solver and suitable boundary conditions to simulate a 3D geometry of the photocatalytic reactor with all energy transport mechanisms.

Post-Processing The velocity was sampled on five different locations in the reactor. The location of the probes can be seen in Figure 4.5. At the current stage of the work, there was no experimental data available to validate the results from the simulation.

Optimization Potential There are two main areas for improvement for the simulation set up, firstly the inclusion of the radiation heat transfer and secondly the implementation of a reaction source term. For the first, the necessary know-how is available in.house, as described in chapter 4.5.1.1. Secondly the inclusion of the photocatalytic reaction should be considered. The integral scalar transport equation [15] describing the scalar transport property ϕ includes a source term S_ϕ that originates from chemical reactions. Since the reaction only occurs on the the phase boundary interface where the catalyst is fixed, a boundary condition for the source term should be implemented to include the photocatalytic surface reaction. In equation (4.19) is t the time, ρ the density, ϕ the physical property, V the volume, $\mathbf{u}$ the velocity vector, Γ the Diffusivity and S_ϕ the source of the physical property ϕ. $\frac{\partial}{\partial t}\rho\phi$ is the transient contribution, $\nabla\cdot\left(\rho\phi\mathbf{u}\right)$ the convection

term, and $\nabla\cdot(\Gamma\nabla\phi)$ the diffusion term [15, 83]

$$\int_V \frac{\partial}{\partial t}\rho\phi\,\mathrm{d}V + \int_V \nabla\cdot\left(\rho\phi\mathbf{u}\right)\mathrm{d}V = \int_V \nabla\cdot(\Gamma\nabla\phi)\,\mathrm{d}V + \int_V S_\phi\,\mathrm{d}V \tag{4.19}$$

Diffusion Contributions

Due to the very small flow velocities in the photocatalytic reactor, the convection times are very large and thus, the Pècelt number is very small. The fluid transport problem is no longer convection dominated and the diffusion contribution must be considered in the scalar transport equation (2.17). The partial differential framework supplied by Aspen Custom Modeler® was used to solve the scalar transport equation in a transient simulation. Figure 4.8 demonstrates the solvability of the problem. The model can be included in any of the other model, however steady state upstream diffusion flow is only solvable with a pseudo-steady state finite differences method if the equation system that solves the system od linear equations iteratively until a pseudo-steady state is reached. Therefore, the process simulation in Aspen Custom Modeler® will become transient, if this model is included in any of the flowsheet variants and thus was not used so far.

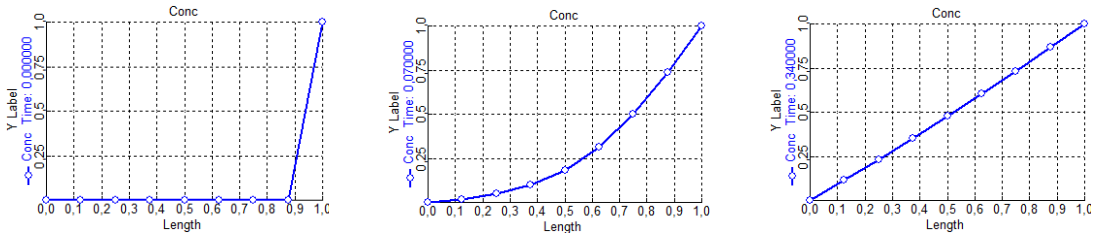

(a) Initial concentration distribution.

(b) Intermediate concentration distribution.

(c) Pseudo-steady state concentration contribution.

Figure 4.8: Diffusive mass transfer concentration plots in Aspen Custom Modeler® .

4.5.2 Photocatalytic Packed Bed Reactor

During the time this work was concluded, changes have been made to the photocatalytic reactor and a second design was proposed with three main differences to the free stream photocatalytic reactor. Firstly, the photo catalyst is fixed on a porous support. Secondly, the inlet feed does not enter the reactor as batch charge and instead is continuously supplied evenly along the reactor length. Thirdly, the reactor concept can no longer be characterized as a plane plate in a longitudinal flow and instead must be characterized fluid flow through porous media. The Aspen Custom Modeler® model used in this work was implemented in connection with the FlowPhotoChem project. Although debates have been conducted, the final implementation modelling choice was

not part of this work and therefore only the literature basis [84] for the model is referenced for reasons of comprehensiveness.

The model is derived from the steady-state tubular reactor with heat exchange. The Aspen Custom Modeler® partial differential equation framework is used to numerically solve the 1D ordinary differential equation along the length of the reactor. The temperature of the reactor is solved as global energy balance. The differential equation derived describes the reactor with the species mole balance F_i as the dependent variable and and the catalyst weight W_cat as the independent variable expressed in the Leibniz's notation as $\mathrm{d}F_i/\mathrm{d}W_{\mathrm{cat}}$.

4.6 Implementation of an Absorption Column in Aspen Custom Modeler®

After the intermediate product stream exits the photocatalytic reactor, unreacted carbon dioxide must be removed from the exit stream of the photocatalytic reactor for the following CO electrolyser. While it is to be expected that there are purity requirements for the feed stream in the subsequent carbon monoxide electrolyser, the requirement has not been quantified yet. Thus, a generic approach has been taken in this work to provide an adjustable solution to this task. An absorption column has been implemented for the purification process. Aspen Custom Modeler® provides a generic absorption column model with a demo case. However, the demo case proved to be unusable without modifications in the current software version. Therefore, a simple representation of an absorption column was implemented. As introduced in the theory (see chapter 2.2.5) absorbate and absorbent are brought into contact multiple times in a counter flow configuration. At each contact, a vapor-liquid equilibrium will develop and absorbate will be absorbed in the absorbent. The overall absorption efficiency and the purity of the product depend on a variety of design factors such as process fluids, e.g. selection of solvent, the geometry of the column, e.g. diameter, number of transfer units, reboiler and reflux ratio and others. The design optimization can be performed once the feed gas requirements are determined.

In each flowsheet, an absorption process with two transfer units has been implemented. The configuration can be seen in figure 4.9. The number of transfer units can be extended to any number of transfer units to achieve higher separation efficiencies. The solvent feed (absorbent) is introduced at the top of the column, the gas feed (absorbate) is introduced at the bottom. Each transfer unit is represented by a vapor-liquid equilibrium flash with the tops of the lower transfer unit (B16) introduced as feed stream (S34) in the upper transfer unit (B18) and the bottoms of the upper transfer unit (S37) introduced as feed stream in the lower transfer unit to ensure counter flow. The absorbate can then be stripped from the absorbent in a regenerator (B14). The units B13 and B17 add the feed and product streams, respectively to check for mass configuration in B15. The overall separation efficiency of the absorber can be determined component-wise for carbon monoxide and

carbon dioxide in B22 (preserved CO percentage) and B12 (absorbed CO percentage), respectively and overall in B26. The overall separation efficiency in B26 can be utilized as objective function (mode maximize) to globally optimize the absorption column with the component mole flow $\dot{n}_i$ for carbon monoxide and carbon dioxide in the tops and the bottoms of absorption column.

$$w = \frac{\dot{n}_{\text{CO, tops}}}{\dot{n}_{\text{CO, bottoms}}} + \frac{\dot{n}_{\text{CO2, tops}}}{\dot{n}_{\text{CO2, bottoms}}} \tag{4.20}$$

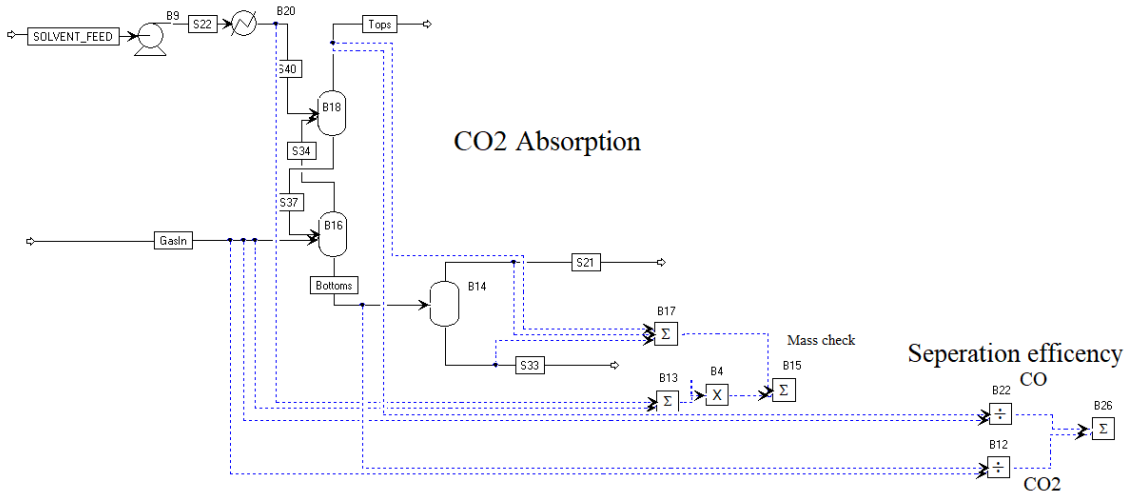

Figure 4.9: Configuration of two vapor-liquid equilibrium flash columns in counter flow configuration to represent an absorption column.

4.7 Miscellaneous Submodels and Extensions

During the work user defined structures, variable types, ports and streams have been defined. All necessary models and sub-models are included in the library with the exception of the heat integration visual basic script since these can not be included in the library.

4.8 Flowsheet

The process simulation in this work has been carried out in Aspen Custom Modeler® . Currently, there are two variants considered in the FlowPhotoChem project. The first variant consists of three reactors serially arranged to produce the desired ethylene as target product from water and carbon dioxide with concentrated solar irradiation input into two of the reactors. Firstly, a

Photo-Electrochemical Proton Membrane Water Electrolyser (PEC-PEMWE) is used to produce hydrogen from water splitting. Secondly, a photocatalytic reactor is used to produce carbon monoxide from carbon dioxide and the produced hydrogen from the PEC-PEMWE reactor and thirdly, an Electrochemical Carbon Monoxide Reduction (EC-COR) reactor is used to reduce the carbon monoxide to ethylene and byproducts. The second variant was introduced in a later stage of the project and consists of two serially arranged reactors. The first reactor is the Photo-Electrochemical Carbon Dioxide Reduction (PEC-CO2R) reactor that reduces carbon dioxide to carbon monoxide. It is a variant of the PEC-PEMWE reactor. The second reactor is the identical EC-COR reactor from the first process variant to reduce the carbon monoxide to the desired ethylene and the same byproducts. Furthermore, for each variant one flowsheet has been implemented that depicts the state of the project and the reactor capacities as of the date this thesis was worked on and one that shows a scaled flowsheet to meet the target of 150 kg/a production target.

General Remarks on the Flowsheets At the current state of this work, pressure losses occurring during the operation of the reactors have not yet been specified. However, pumps and heat exchangers are included in each flowsheet at stages where one would expect pressure change utilities or heat exchangers. Both utilities have been implemented with the predefined models in the dynamics library of Aspen Custom Modeler® . Per default configuration each of the two utilities are specified with a fixed duty, electrical or thermal, respectively. The specification states were changed from fixed to free for all heat exchangers and pumps. Pressure and temperature are always fixed in the stream downstream of the utility if one is used or downstream of the second utility if both are used sequentially.

The pre-defined model for material streams in the Aspen Custom Modeler® library includes a global component list containing all species present in the material stream as well as one inlet and one outlet component list. Generally, the inlet and outlet component lists are initialized with the global component list of the stream. However, if it was necessary to switch between component lists, this has always been done in the outlet material stream component list. If the outlet component list includes components that are not included in the inlet component list, the outlet mole fraction has been specified as fixed and set to zero for each component not included to square the simulation. The terminology to square the simulation is used to describe a well specified state of the flowsheet. The expression is derived from the requirement that an equal number of equations and calculated variables must be specified. This is necessary for the capability of the software to adapt the order in which the equations are solved from the variables that are specified by the user to be calculated. This allows for a very versatile adaption of the flowsheet to changes of the boundary conditions of the process.

Each flowsheet has mass conversation checks implemented at the current stage. While these should be removed for the final version, it has been found very helpful during the modeling process since the convergence of a flowsheet does not automatically ensure mass conservation if the problem is

specified poorly.

It should be noted that the objective of an ethylene production target of 150 kg/a is subject to the following conditions. The production target is calculated based on 24 h/d and 365 d/a operation time. Consequently, this does not depict reality for a number of planned and unplanned downtime of a production facility:

- Planned maintenance such as cleaning and operational safety checks
- Unplanned downtime such as human, hardware and software errors

Furthermore, the concept is strongly reliant on the weather conditions due to the concentrated solar power for the photocatalytic reactor and the photovoltaic cells for the electrical power of the PEC reactors. In 2008, on average 840 and 1010 annual full load hours have been reported for Hamburg and Munich, respectively [85]. While these numbers are very much subject to the latitude of the production plant, 24 hours of sunshine per day for 365 d/a is self evidently not achievable. However, the quantity of ethylene production per year highly depends on the location of the plant, the continuous progress achieved in increasing the efficiency and decreasing in contingency risk. Calculating the production volume of the plant with 8760 annual full load hours allows for a straightforward scaling for the three previously listed dependencies of the expected production volume of ethylene per year using equation (4.21) if data for the practically achievable full load hours for the plant is available.

$$\dot{m}_{C_2H_4,\text{expected}} = \frac{\text{annual full load hours}}{8760} \dot{m}_{C_2H_4,\text{full load}} \tag{4.21}$$

In the following paragraphs, each flowsheet variant and the choices for the process configuration are explained. Some process choices also apply for the following flowsheet, however, in order to avoid repetitions they are only introduced in the first flowsheet.

Current State PEC-PEMWE, PC, EC-COR Figure 4.10 shows the configuration for the variant of three reactors at currently demonstrated capacity. The reactors used are one PEC-PEMWE reactor, one PC reactor, and one EC-COR reactor. The flowsheet has been implemented such that each reactor is operated with the currently experimentally achievable feed streams. The PEC-PEMWE reactor unit is an electrically and thermally integrated PV-module for operation under concentrated solar irradiation with a PEM water electrolyser. The electrolyser is connected with the GaInP/GaInAs/Ge triple junction concentrated PV cell with 24 serial and 4 parallel cells and without cooling with an electrical stream (electrical efficiency of unity). The electrical

operating point is determined by the intersection of both current-voltage curves and is a function of the solar irradiation, the temperature and the pressure. For anode product stream of the PEC-PEMWE reactor the vapor liquid equilibrium is calculated and the excess oxygen produced from the oxygen evolution reaction is discharged before the anode stream is recirculated to the anode inlet. The cathode products are mixed with an external carbon dioxide stream to form the reactants feed mixture for the photocatalytic reactor (PC). The carbon dioxide feed stream is dynamically initialized with a constant CO_2/H_2 ratio of unity to match the reverse water gas shift reaction (R9) stoichiometry. The feed mixture is then introduced to the photocatalytic reactor with a feed rate of $6.96 \cdot 10^{-5}$ kmol/h. This value corresponds to the current lab value under investigation. The excess hydrogen feed from the PEC-PEMWE is split off in B7. The calculated overproduction ratio between the split off stream and the photocatalytic reactor feed at the current state of the project is 21.71[1]. The control blocks B23 and and B25 check for mass conservation of the reactor. The products are cooled in the heat exchanger B19 to a temperature of 5 °C before entering the lower transfer unit B16 of the absorption column. The control block B15 configuration checks for mass conservation. B12, B22 and B26 evaluate the overall absorption column efficiency which was used to optimize the solvent feed to maximize the carbon dioxide in the bottom and the carbon monoxide in the top fraction. The solvent feed introduced at the upper transfer unit B18 of the absorption column contains a KOH/H_2O mixture with a ratio of 0.5. The absorption column is operated at a constant temperature of 5 °C and a pressure of 1 bar. The bottoms are flashed to strip the absorbate (CO_2) from the absorbent (KOH/H_2O mixture). The tops are mixed with water to form the feed stream for the electrocatalytic reactor for the CO reduction. In the flowsheet, the EC-COR reactor is coupled with the aforementioned triple junction concentrated PV cell with a different configuration than in the PEC-PEMWE reactor. Under lab conditions, the reactor has no PV-module integrated. The PV module is purely connected in the flowsheet to demonstrate the necessary sizing if a PV module were to be connected, which was part of the latest change request. Thus, instead of calculating the intersection of current-voltage curves, the PV module is specified such that does not influence the operating point of the ECCOR reactor. The electrolyser is operating at a fixed current density of $0.3\,A/m^2$ and the PV cell is specified with one serial cell. Two parallel number of cells are calculated to meet the electricity demand of the EC-COR reactor. The area of the electrolyser is specified as free and calculated such that the mole fraction of carbon monoxide in the product stream is equal to zero corresponding to complete carbon monoxide conversion.

[1] With the current production volume of the PEC-PEMWE, this value is 217.1. For explanation please refer to the chapter 5

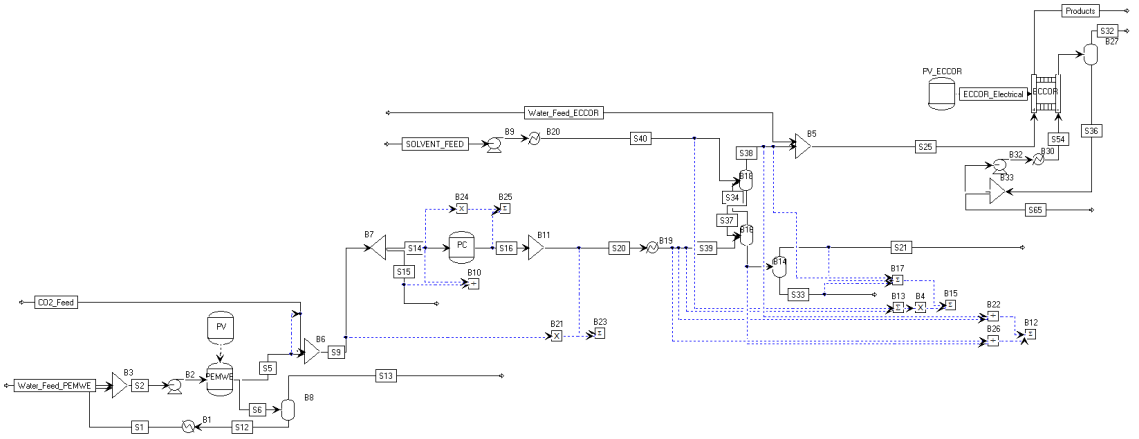

Figure 4.10: Flowsheet for the PEC-PEMWE, PC and EC-COR reactor variant for the current state of the experimental reactor capacities.

Target 150 kg/a ethylene PEC-PEMWE, PC, EC-COR Figure 4.10 shows the flowsheet for the concept using three serially arranged reactors, PEC-PEMWE, PC and EC-COR for the ethylene production target of 150 kg/a. Since the process flowsheet was derived from the previously discussed flowsheet (see figure 4.11) for the current state of the experimental reactor capacities, only the adaptations that have been made from the previous flowsheet will be discussed in the following paragraph. A parallel configuration for the photocatalytic reactor was chosen to match the hydrogen overproduction from the PEC-PEMWE reactor such that the flowsheet adapts dynamically and progress is made in the experimental performance and can be tracked without changing the structure of the flowsheet. To achieve this, one photocatalytic reactor was included in the flowsheet to determine the product composition, temperature and pressure at the reactor outlet. To simulate the parallel reactors, the feed stream S27 is specified with the molar flow ratio between the PC reactor inlet stream S14 and the split-off stream. The composition, temperature and pressure in the feed stream S27 are initialized with the values from the outlet stream S16 of the PC reactor and mixed with S16 in the Mixer B11. To adjust for changes in the reaction kinetics, one should adapt the reaction structure *PhotoThermalRuSTO*. The number of parallel photocatalytic reactors decreases for increases in the PC reactor feed stream under laboratory conditions. To adjust the feed stream capacity, one should change the molar flow rate in S14 accordingly. If either the product stream composition at the end of the PC reactor changes due to changes in the reaction kinetics or the feed flow rate one should optimize the adsorption column using the separation efficiency in B26 as objective function and the specified solvent molar feed stream as decision variable.

The tops from the absorption column are mixed with a make-up stream before the EC-COR reactor. In the current form of the flowsheet the molar component flow of ethylene is fixed at the target value of 150 kg/a in the product stream of the electrolyser and the area of the electrolyser set as a free variable to scale the electrolyser to match the target ethylene production. If excess carbon monoxide is introduced to the electrolyser, the performance of the electrolyser will not be influenced since no mass transport effects are currently included in the implementation of the

model. However, if less carbon monoxide is in the feed stream of the EC-COR reactor than it is required by the specified production target, the solver will abort the simulation since the solver would try to solve for a negative molar flow. However, the lower bound of a molar flow type variable is set to zero in Aspen Custom Modeler® to avoid unfeasible solutions and causing the solver to abort. Therefore, the make-up stream before the EC-COR reactor was implemented with a H_2O/CO ratio of 0.5 since only too little but not too much carbon monoxide influences the simulation results of the reactor in case of the currently implemented simplified reactor module. To check if the feed stream supplied from the photocatalytic reactor does satisfy the carbon monoxide demand of the EC-COR reactor, the control block B34 was introduced. If the difference between the carbon monoxide in the feed and product stream, which corresponds to the net conversion rate of carbon monoxide in the EC-COR reactor, is greater than the carbon monoxide in the tops of the absorption column, the output signal of the control block B34 will become negative. The ratio between the net conversion rate of carbon monoxide in the EC-COR reactor and the molar carbon monoxide flow rate in the tops absorption column can be used as global scaling factor for the full flowsheet.

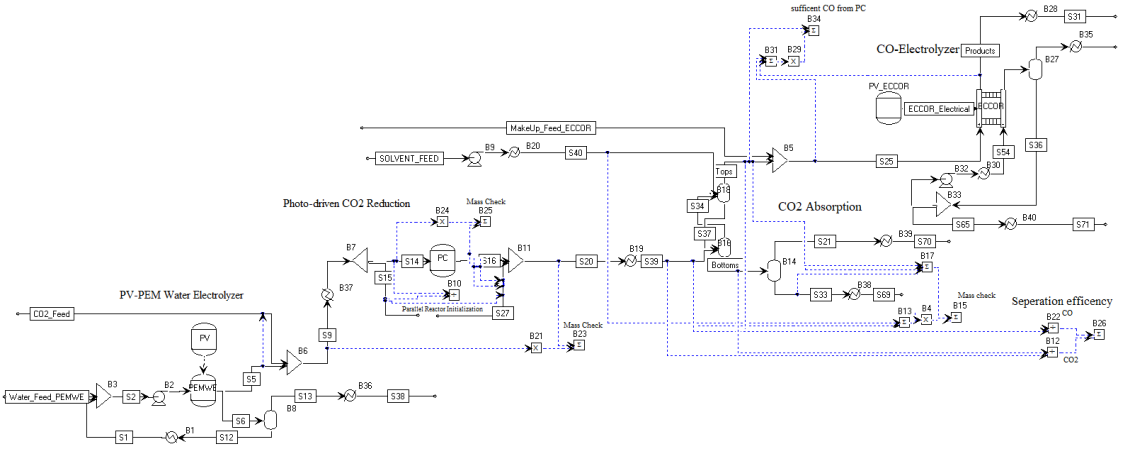

Figure 4.11: Flowsheet for the PEC-PEM, PC and EC-COR reactor variant for the production target of the project of 150 kg/a ethylene.

Current State PEC-CO2R, EC-COR Figure 4.12 shows the configuration with the serially arranged reactor for the photo-electrochemical reduction of CO_2 (PEC-CO2R) and the electrochemical reduction of CO (EC-COR). In the flowsheet, both reactors are coupled with a GaInP/-GaInAs/Ge triple junction concentrated PV cell with the exception that the PEC-CO2R reactor is also thermally integrated through the water stream passing the PV module firstly and the anode of the electrolyser secondly. The control units B5, B6, B7 and B8 check for mass conservation in the PEC-CO2R reactor. The cathode outlet stream is fed towards the absorption column with two numbers of transfer units B31 and B13. The tops of the absorption column are mixed with water and then introduced into the CO reduction reactor. In the experimental set-up, the EC-COR reactor is not connected to a PV cell. In the review process of the flowsheets it was requested to also

connect the EC-COR reactor to a PV cell. Thus, in the flowsheet the EC-COR reactor is connected to a triple junction concentrated PV cell with one parallel cell. The configuration of both PV modules follows the identical logic described in the target PEC-PEMWE, PC, EC-COR flowsheet and the number of serially connected cells is calculated from the electrical power demand of the EC-COR reactor operated at a specified current density. In this configuration, the PV cell does not have any influence on the performance of the EC-COR reactor and only provides the specification of the size of an installation if the reactor would be connected to a triple junction concentrated PV cell. The control units B2, B11 and B13 calculate the overall absorption efficiency as the mole flow of carbon monoxide in the tops and the carbon dioxide in the bottoms divided by the inlet mole flow of the component, respectively. The control units B17, B18, B21, and B23 check for mass conservation.

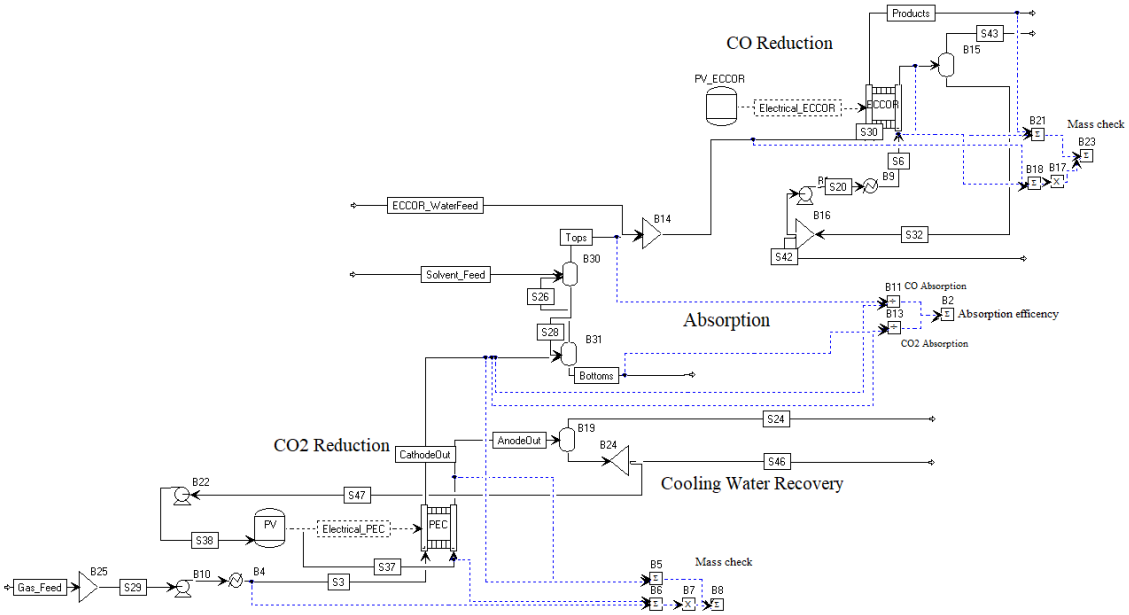

Figure 4.12: Flowsheet for the PEC-CO2R reactor and EC-COR reactor variant for the current state of the project.

Target 150 kg/a ethylene PEC-CO2R, EC-COR The overall design of the process for the target ethylene production of 150 kg/a differs very little compared to the current state flow sheet presented in the previous section. In the following, the differences to the current state flowsheet are highlighted. The EC-COR reactor feed stream consists of carbon monoxide and water ratio of 1:2 instead of pure water. The product flow rate at the EC-COR reactor outlet is fixed to match the ethylene production target value of 150 kg/a and the area of the electrolyser is left as free variable.

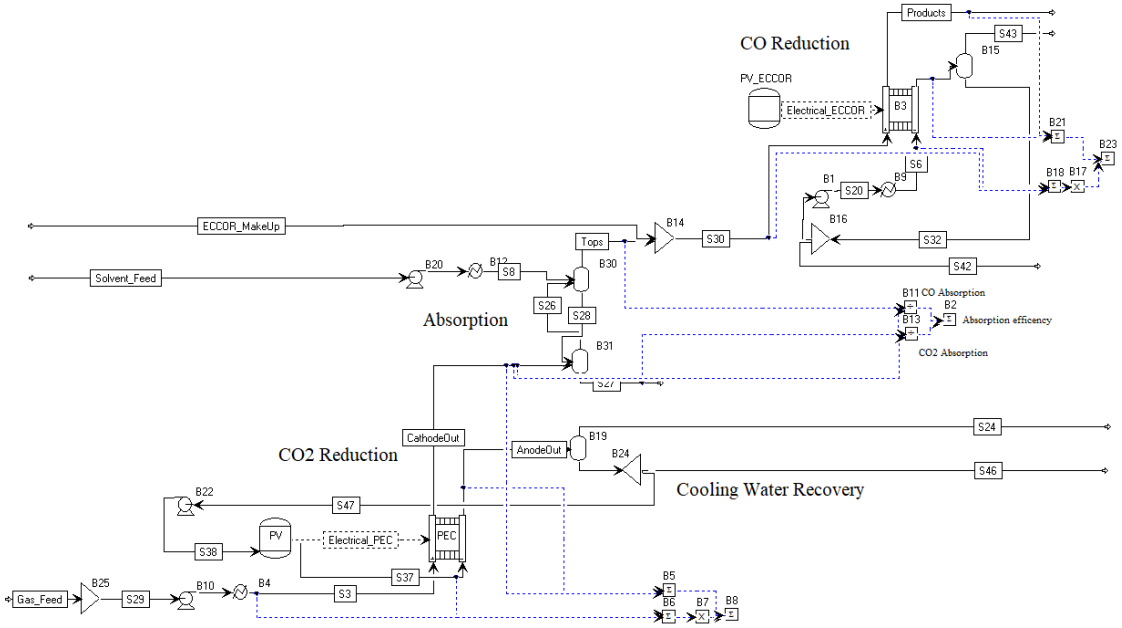

Figure 4.13: Flowsheet for the PEC-CO2R and EC-COR reactor variant for the ethylene production target of 150 kg/a.

4.9 Heat Integration

Heat exchangers have been implemented for all of the four flowsheets. Once the reactor models are fully dependent on the operating conditions of temperature and pressure, each reactor can be optimized globally with the objective to maximize the ethylene conversion efficiency. To perform the heat integration, an in Aspen Custom Modeler® universally applicable Visual Basic Script was implemented that accumulates all necessary data for any given flowsheet. The data will be written in a provided excel sheet. The data output is structured such that it complies with the format required by the Aspen Energy Analyzer® V10. The Source Code 4.3 shows the important lines from the code. The algorithm loops through each block in the global block collection of the flowsheet and checks if the utility type is a heater and loops each port connected to the block.

Source Code 4.3: Visual Basic script to export from Aspen Custom Modeler® to Aspen Energy Analyzer® for the heat integration

```
set blkColl = Blocks                                                    33
for each b in blkColl                                                   34
  if b.TypeName = "Heater" Then                                         35
    with b                                                              36
      ws.Cells(i,1).Value = .Name                                       37
      ws.Cells(i,2).Value = "1"                                         38
      ws.Cells(i,3).Value = b.T_in.value                                39
      ws.Cells(i,4).Value = b.Out_P.T.value                             40
      ws.Cells(i,6).Value = .hin.value                                  41
      ws.Cells(i,8).Value = 720                                         42
      ws.Cells(i,10).Value = .F.value                                   43
```

```
      '.Cells(3,11).Value = "Effective Cp"
      ws.Cells(i,12).Value = "Global"
    end with
    i = i+1
  end if
next
```

4.10 Software

For this work, different software has been used to simulate the desired process. For the overall process simulation, the Aspen® software Aspen Custom Modeler® V10 has been used with a combination of user defined models for the reactors itself and predefined unit operations and calculation procedures, such as vapor-liquid-equilibrium flash columns, material streams, pressure changers and heat exchangers from the built-in Aspen Custom Modeler® dynamics library. Because the implementation in Aspen Custom Modeler® is time consuming since variable values are not as easily accessible and plots are more time consuming to be implemented, reactor models have been developed separately using the `julia` [44] programming language.

Since experimental data has been rarely accessible, especially for the photocatalytic reactor, an OpenFOAM® simulation has been implemented to clarify the flow behavior of the reactor. The CFD simulations were performed using the open source software OpenFOAM® v6 [15]. Different meshes for the CFD simulation have been created with the NETGEN 1D-2D-3D algorithm in Salome. The OpenFOAM® utility `chemkinToFoam` [83] has been used to initialize the transport and thermodynamic files in the *constant* directory. The post processing has either been performed directly with OpenFOAM® utilities or ParaView. All further information in the OpenFOAM® simulation can be found in chapter 4.5.1.1.

4.11 Thermodynamic Data

Thermodynamic data has been mostly obtained via the physical property methods in Aspen Custom Modeler® by accessing Aspen Properties. For all other data, the following data basis has been checked.

- NIST Webbook [86]
- NIST JANAF Thermochemical tables [87]
- Gri-Mech 3.0 files [18]

4.12 Best Practices for Aspen Custom Modeler®

During the simulation of the process, several learnings and observations have been made, that were not apparent from or generally included in the official Aspen Custom Modeler® documentation. To document and transfer the knowledge for further work in this project or in related projects, these observations and learnings will be briefly summarized in this chapter.

- To avoid unnecessary usage of storage, it is recommended that with the creation of a new version, e.g. as a backup copy it is recommended to clear the snapshots that are automatically generated, since with the creation of a new version, all previous snapshots are also copied to the new simulation.

- Sometimes, convergence issues can occur, if material streams are not initialized. This happened predominantly when implementing vapor-liquid-equilibrium flash blocks. In most cases, it has been found beneficial to first introduce the material feed streams on the flowsheet, initialize each feed stream with the configuration user interface from Aspen Custom Modeler® and only then, after each stream set-up was successful, to introduce the flash block, connect the feed streams to the flash block and run the simulation.

- If vapor-liquid-equilibrium flash columns are configured in a counter flow set-up, it has proven beneficial to initialize two identical solvent feed streams, connect each to one flash column, run the simulation and then connect the counter flow configuration.

- If simulations failed to converge, values should always be reset to the last snapshot. Often, the variable values resulting from the diverged run caused the simulation to diverge again with flowsheet specifications that did solve if the values were reset.

- Aspen Custom Modeler® offers for implementation of the chemical reactions the Aspen Reaction Toolkit. While this toolkit has been found to be very helpful, it only offers predefined input for the typical reaction kinetic descriptions, such as the power law or Langmuir-Hinshelwood kinetics. The Aspen Reaction Toolkit can be accessed in the user defined models for variable information such as stoichiometric coefficients. Furthermore, the Aspen Reaction Toolkit offers the implementation of a custom reaction kinetics using the Aspen Reactions Wizard for the initialization of the user defined model files. However, problems have been found and were confirmed by the Aspen Support Center causing the software to

shut down when using the Aspen Reaction Wizard. It has been recommended by the Customer Support to migrate to the Aspen® V12 products, since Aspen Custom Modeler® V10 will no longer be further developed. If the version V12 shuts down when the Aspen Reaction Toolkit is used, the methodology to check whether it is the same error as in V10 is the following. The Aspen Custom Modeler® creates a variable name *UPPER* in the code. This error will cause the software to shut down. Since this error occurs in the part of the code that is not supplied by the user, the variable name *UPPER* is not visible in the Custom Modeler and only if the Aspen Custom Modeler® File is opened with a text editor such as *Notepad++*.

- Simulation data can be exported using VBA-Scripting. While it is good practice in VBA FOR-loops to reference the variable that is subject to the increment, Aspen Custom Modeler® aborts with an error and can only handle NEXT end of the FOR-Loop

- Often, using the homotopy option in Aspen Custom Modeler® it is necessary to change from one simulation state to another

5 Results and Discussion

5.1 CO/CO2 Recovery Process Comparison

In both process variants presented in chapter 4.8, unconverted carbon dioxide must be separated from the intermediate product carbon monoxide to meet the feed specification of the EC-COR reactor. While there are multiple processes available such as absorption, adsorption, distillation, and membrane separation each process has advantages and disadvantages which will be discussed.

Often, membrane separation technologies are undesirable due to economic considerations. Favre [88] reported for carbon dioxide capture with membrane technologies that membrane separation technologies are only economically competitive at inlet concentrations greater than 20 % carbon dioxide. Recently, Yang et al. [40] reported that at a cost of 45 \$/t CO_2 - 80 \$/t CO_2 membrane technologies are economically competitive with amine processes. For both technologies a variety of techno-economic analyses have been performed [89–99]. Cryogenic distillation has been used in olefine plants for more than 60 years, respectively to the publication date for now 70 years [100]. The separation is performed at very low temperature, which results in very expensive operational expenditures, since it is highly energy intensive [100]. Furthermore, cryogenic distillation often faces difficulties in freeze up in the column if there are species with a freezing point greater than the boiling points of the two fractions that are to be separated which define the operating point. For example, carbon dioxide must be removed completely before carbon monoxide can be separated from other components [101]. Thus, cryogenic distillation is not only expensive, but might also require much greater separation efficiencies to avoid freeze up than would be required by the feed specification to the following reactor. Therefore, cryogenic distillation can possibly severely limit the efficiency of the process.

Adsorption processes require a solid that physically or chemically adsorbs the molecules on the surface and must be regenerated or exchanged to maintain the separation efficiency. In both cases, this can be done for continuous and discontinuous operation with the only difference whether the adsorbent can be regenerated. If the adsorbent can not be regenerated, finding a cheap adsorbent is critical to the economic feasibility of the process. Firstly, a discontinuous operation of the plant can separate the feed until the capacity of the adsorption solid is reached. Then, the plant will be shut down and the carbon dioxide desorption process can be performed to regenerate

the adsorption medium. However, this will result in a decreased separation efficiency since the capacity decreases with time. The separation efficiency should be checked against the feed requirement of the following EC-COR reactor. Secondly, the process can be operated continuously, by pneumatically transportating the adsorbent in form of fluidized particles. This avoids the time dependent separation performance.

Alternatively, a fluid absorption process can be chosen. In comparison to the fluidized bed adsorption, it is easier to achieve a homogeneous distribution of both phases. Absorption processes are widely and mainly used throughout downstream processing for the separation of carbon dioxide. Matrillo evaluated for the year 2012, that the technologies used in downstream carbon dioxide removal in biogas plants were upgraded. Water and chemical absorption processes have been reported with a cumulative number of 118 installations, membrane separation with eight, amine absorption with seven and cryogenic process units with six installations [102, 103].

Therefore, an absorption column was used for the removal of untreated carbon dioxide, but arguably, membrane technologies are an attractive alternative and overall should be evaluated if the carbon monoxide purity requirements for the EC-COR reactor are specified by the external partner. The US patent on the removal of carbon monoxide with a membrane reported a carbon monoxide yield greater than 90 wt-% [104]. A second patent on the removal with an absorption process reported a product gas purity of 98 % carbon monoxide in their process configuration. The COSORB® absorption process achieves purities exceeding 99 % [105], but it is not clearly quantified whether mole or weight percentages are provided. The Kinetics Technology International corporation owns the proprietary COSORB® process which is based on the complexation and decomplexation in a dissolved organic cuprous aluminum chloride mixture. One advantage of the COSORB® process is that it can handle methane in the feed stream, which is a by-product of the photocatalytic reactor used in this work. Several amine scrubbing processes are patented for the carbon dioxide removal, including monoethanolamine (MEA) and diethanolamine (DIPA) [106]. While the choice of unreacted carbon dioxide removal for the process simulation in this work has been an absorption column, it should be noted that this choice only reflects the decision of the author to implement the separation of unreacted carbon dioxide in the current configuration by using an absorption column and not the choice of the FlowPhotoChem project.

This demonstrates that a variety of possible gas separation technologies are currently available to achieve the separation of unreacted carbon dioxide form carbon monoxide. The final selection of the separation technology depends on a variety of criteria. Firstly and most importantly, it will depend on the components present in the stream that are to be separated since the PC reactor outlet stream contains methane as product, which can be handled by e.g. the COSORB® process. Both reactor concepts contain untreated carbon dioxide which will be problematic in cryogenic distillation separation to separate pure carbon monoxide as previously discussed. Secondly, the selection depends on the composition of the feed stream and thus on the selectivity and conversion of the preceding reactor, and the temperature of the feed stream to utilize the temperature level of the preceding reactor to minimize operational expenditures. Thirdly, the purity that needs to

be achieved after separation is important in determining the technology. Fourthly, the selection of the gas separation technology should depend on the capital and operational expenditures of the technology since the technologies listed above are normally deployed on an industrial appliance for commercial usage. For smaller scale operation, the economic feasibility must be reevaluated.

In this work, four absorbents, namely DIPA, MEA, KOH, and water, have been tested with one transfer unit in the absorption process to determine the overall performance of the absorption efficiency of each solvent and to test the numerical stability of the calculations. For the process simulation in Aspen, the recommended physical property model for electrolyte containing Non-Random-Two-Liquids (ELECNRTL) was chosen.

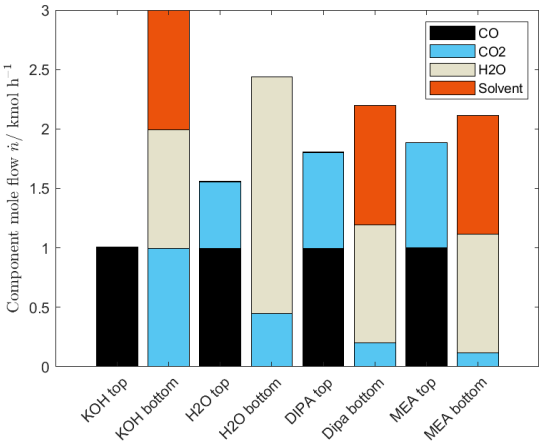

Figure 5.1: Overhead and bottom composition of the single stage absorption process with monoethanolamine (MEA), diethanolamine (DIPA), potassium hydroxide (KOH), and water.

Figure 5.1 shows the composition of the overhead and bottom stream for each solvent. Figure 5.2 shows for each component the mole flow in the bottom (indicated as the negative value in the chart) and the mole flow in the overhead stream (indicated as the positive value in the chart). For all four solvents the carbon monoxide is exclusively present in the overhead stream and the solvent in the bottom stream. For the carbon dioxide removal the absorbents MEA, DIPA, water, and KOH rank from least effective to most effective with a molar carbon dioxide flow rate in the tops of 0.88 kmol/h, 0.80 kmol/h, 0.56 kmol/h, and 0.001 kmol/h, respectively. The corresponding weight percentages of carbon dioxide removed from the feed are 11.6 wt-%, 19.8 wt-%, 44.4 wt-%, and 99.4 wt-%, respectively. The maximum amount of carbon dioxide that can be absorbed in aqueous amine solutions expressed as weight percentage of absorbed carbon dioxide relative to pure MEA and DIPA is approximately 25 wt-% [107]. The weight percentage achieved in the single stage absorption is 6.5 wt-% for DIPA and 8.3 wt-% for MEA. Considering that maximum weight percentage is given for an absorption column, the numbers are in the expected range.

However, the weight percentages achieved with pure water as solvent are unreasonably high and should be further investigated. Experimental data from Duan and Sun [108] reported experimental values of less than 0.5 mol/kg. Since the purity requirement for the EC-COR feed has not yet been specified, KOH was chosen as solvent because it showed the best separation performance. However, potassium hydroxide being more expensive than the other three solvents and if the threshold value for the carbon dioxide percentage in the feed stream can be achieved with any of the other solvents, it is economically more feasible to adapt the absorption process accordingly. Each flowsheet has been implemented with KOH as solvent, and water and DIPA can be selected as alternative solvent. If the homotopy option in Aspen Custom Modeler® is activated for the specified solvent feed, the solvent can be changed for any simulation in this work.

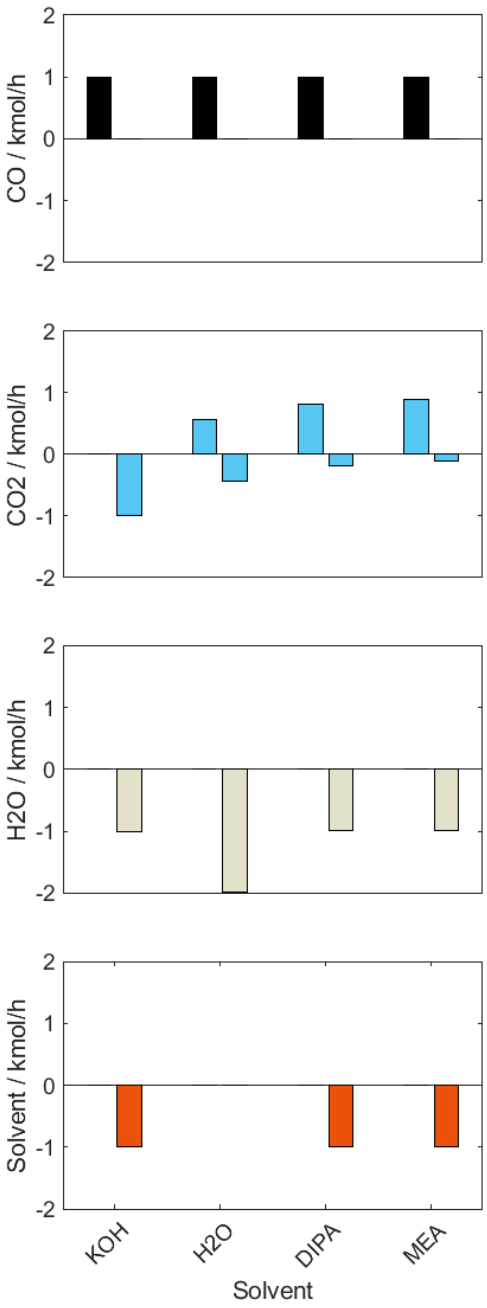

Figure 5.2: Composition of the top and bottom streams for the absorption solvent options monoethanolamine (MEA), diethanolamine (DIPA), potassium hydroxide (KOH), and water.

5.2 Electrolyser Model

In this work, the activation overpotential was fitted to the phenomenological model. While fitting the experimental data to the model, it was found that the result of the parameter optimization problem was sensitive to the initial values and the bounds provided. Table 5.1 shows two different parameter sets leading to one successful and one unsuccessful parameter fit, respectively. Figure 5.3 shows the results for the cell voltage as sum of the reversible voltage, and the ohmic, anode and cathode overpotential as a function of the current density for the two parameter sets in Table 5.1 with only one set correctly matching the experimental data and the physical behavior of the activation overpotential. Since a gradient based optimization algorithm was used, choosing a starting value that is sufficiently close to the final value is critical to find the global optimum and avoid finding local optima. For the parameter optimization in case of the phenomenological model at a constant temperature, this problem was manageable and the fit was successful.

Table 5.1: Optimization parameter sets for the electrolyser overpotential fitting.

Optimization set	Lower Bound	Upper Bound	Starting Value
successful	p_1=0	p_1=0.5	p_1=0.05
	p_2=10^{-12}	p_2=1	p_2=10^{-4}
	p_3=0	p_3=2	p_3=1
unsuccessful	p_1=0	p_1=0.99	p_1=0.01
	p_2=10^{-12}	p_2=1	p_2=0.9
	p_3=0	p_3=20	p_3=15

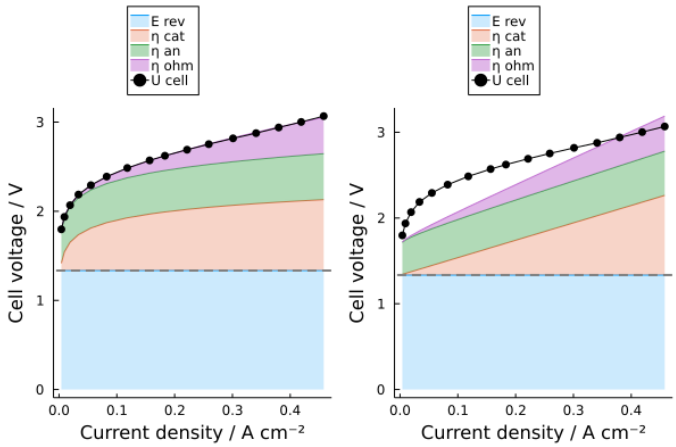

Figure 5.3: Results for the electrolyser model fit for different optimization parameter sets.

However, when it was tried to fit the experimental data from Boutin et al. [72] and from Endrődi et al. [73] for the temperature dependent activation overpotential, the fit remained unsuccessful. Figure 5.4c shows the experimental data from Boutin et al. [72] that has been used and the results of the parameter optimization. The combined data set includes experimental data from Endrődi et al. [73] and from Boutin et al. [72] at different voltages and temperatures. The following initial

strategy was pursued. The experimental data was separated into two sets, one data set to fit the model parameter and one data set to validate the model together with the fitted parameters against data that was not used for the fit. Under the premise of a successful fit, the model should describe the second set accurately. The data from Endrődi et al. [73] was used to fit the model and the data from Boutin et al. [72] was used to test the validity of the model. Figure 5.4a shows the fit for the temperature dependent activation overpotential equation with the experimental data from Endrődi [73]. However, when the parameters from the model fit were used to test the validity of the model, the model predictions did not match the experimental data. The most likely reason for this is the limited amount of data available for the fit. Local overfitting of the fit parameters results in a good data fit for a small temperature range, but when tested against the data excluded from the fitting, the model did not match the experimental data. Upon further inspection, it was found that different starting parameters resulted in equally good data fits but very different parameter values. Considering the difficulties described in the previous section, that the initial parameter values and the bounds contributed greatly to the success of the parameter fit, the problem was addressed using non gradient-based algorithms instead of gradient-based algorithms. Both a genetic algorithm and a particleswarm algorithm tested as alternative did not provide a good fit for the temperature dependent activation overpotential model. Additionally to the optimization algorithms in Julia (see figure 5.4d), the Matlab algorithms were tested as alternative (see figure 5.4c). The reasons for the unsuccessful parameter fit can be manifold. Unsuitable optimization algorithms were chosen for the parameter fit. Assuming the optimizer is suitable, the parameters for the optimizer such as e.g., number of iterations, bounds, initial conditions, number of particles/generations, could be chosen poorly. Also, the experimental data set could be so small and the number of local optima so manifold that the global optimum is not found. As the optimization did not provide the data hoped for, the procedure should be tested with a larger set of experimental values and if the problem is not solved, the parameters for the optimizer should be examined accurately.

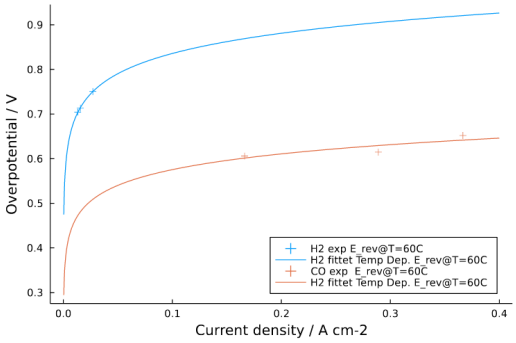

(a) Temperature dependent activation overpotential fit with the experimental data from Endrődi [73].

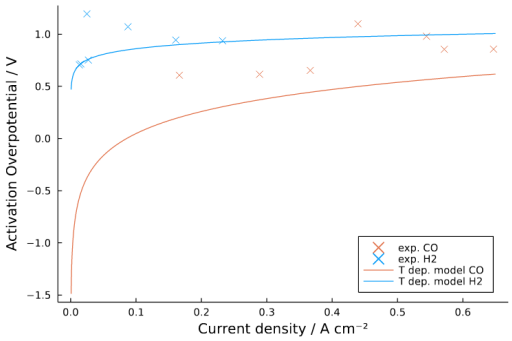

(b) Temperature dependent activation overpotential fit with gradient-based function `curve_fit` for the reduction of CO_2 towards CO with he experimental data from Endrődi et al. [73] and from Boutin et al. [72].

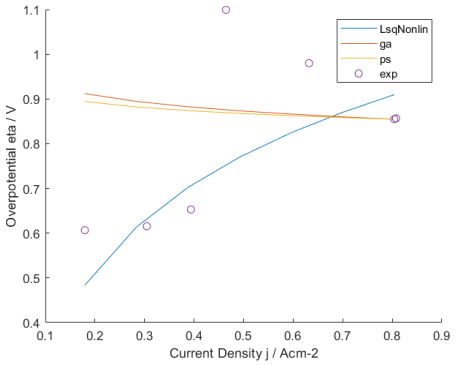

(c) Temperature dependent activation overpotential fit with gradient-based and non gradient-based genetic algorithm and particleswarm in MatLab for the reduction of CO_2 towards CO with he experimental data from Endrődi et al. [73] and from Boutin et al. [72].

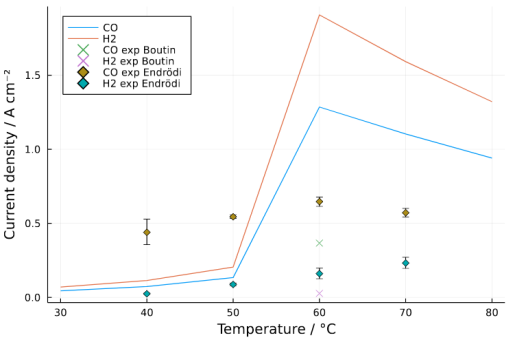

(d) Temperature dependent activation overpotential fit with the non gradient-based `particleswarm` function for the reduction of CO_2 towards CO with he experimental data from Endrődi et al. [73] and from Boutin et al. [72].

Figure 5.4: Results for the temperature dependent activation potential optimization fit.

5.3 OpenFOAM® Simulation for the Photocatalytic Reactor

The initial objective of the OpenFOAM® simulation was to closely examine the flow behavior in the reactor and to demonstrate the feasibility of a computational fluid dynamics simulation and evince the prospect of coupling the diffusion and convection heat transfer problem with the radiation heat transfer from the concentrated solar irradiation, especially since the solar process demonstrator group in the institute has in-house knowledge, boundary conditions and optimized solvers for radiation heat transfer problems in solid-fluid multi-phase heat transfer. Figure B.1 shows the residuals of the OpenFOAM® simulation. If the residual control is activated in the control dictionary, the solver aborts the simulation after less than 1000 iterations since the residuals are smaller then the abort criteria specified by the user. However, due to the very small flow velocities at the inlet the changes in the domain are so slow, that even though the problem is not converged, the residuals become lower than the stopping criteria, although set at 10^{-6}

Figure B.2 shows the Relative mass conservation in the reactor as the difference in the mass flux between inlet and outlet divided by the mass flux in the outlet. The residual demonstrates, that as many as 100,000 iterations are necessary until the problem converges. Figure 5.5 shows the velocity distribution at 2 mm, 2.5 mm, 3.5 mm, 11 mm, and 19 mm. The results demonstrate that the reactor depicts for the greatest part of the reactor laminar flow behavior. The qualitative results or significant, however quantitatively the velocities should be reevaluated after the relative mass residuals are also fully converged. Intermediate results at 60,000 iterations showed in comparison to the results in figure 5.5 changes for the velocities for the 19 mm sampling probe. Overall, the simulation is computationally expensive due to the low velocities in the reactor, however if the problem is coupled with radiation heat transfer and the source term for the photo-driven reaction kinetics described in chapter 4.5.1.1, the OpenFOAM® simulation can provide valuable insights if pursued further.

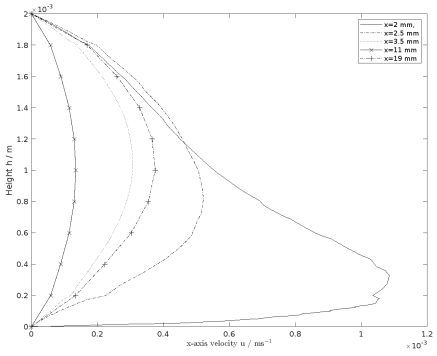

Figure 5.5: X-axis velocity profiles for the photocatalytic reactor CFD simulation with OpenFOAM® .

Figure 5.6 shows the streamlines flow in the disk shaped reactor chamber of the PC reactor. The streamlines are colored according to the x-axis velocity. The photocatalytic flow in the

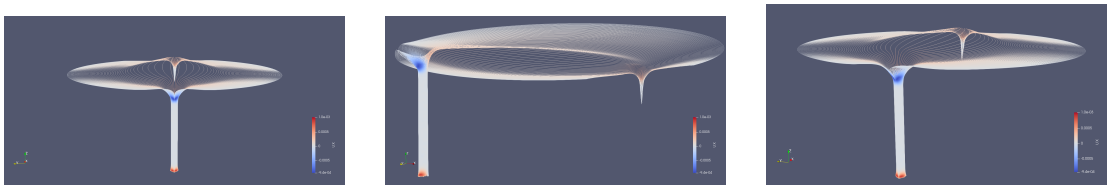

Figure 5.6: Streamline profiles for the photocatalytic reactor CFD simulation with OpenFOAM® .

photocatalytic reactor is distributed homogeneously with no turbulence.

Figure 5.7 shows the x-axis velocity distribution at a cross section on the z-axis normal plane at the center of the disk. The color schemes have been clipped at a maximum velocity of 10^{-4} m/s to better show the differences in the velocities. However, it should be noted that the shown velocity values near the inlet and outlet closer within a radius of approximately 1.5 mm do not show the true velocities and the actual values are expected to be greater. The figure demonstrates a faster flowing channel flow in the center of the disk and up to five times smaller velocities near the edge clearly demonstrating the weakness of this reactor concept. There is a broad residence time distribution and therefore, the residence time for the center of the reactor is too small if a large inlet feed flow is chosen and too large at the edge of the reactor if a small inlet feed flow is chosen. Both result in a sub optimal operation of the reactor.

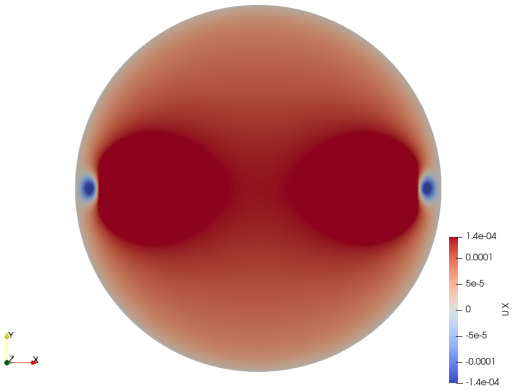

Figure 5.7: X-axis velocity distribution for a cross section on the x-y-plane for the photocatalytic reactor CFD simulation with OpenFOAM® .

5.4 Heat Integration Potential

To determine the heat transfer potential in a heat integration, the hot and cold streams are plotted as composite curves. Figure 5.8 shows the composite curves for the target flowsheet for the 150 kg/a ethylene production target PEC-PEWME, PC, EC-COR reactor configuration. The figure at the

current state shows little potential for heat integration. Currently, the PC reactor inlet stream can be preheated by recovering heat from the hot outlet stream of the PC reactor. The final amount of heat recovery is not quantified in this work since the reactor models have not been optimized in respect of their optimal operation conditions and thus making any quantitative claim for heat integration potential invalid. However, if firstly the operating conditions for each reactor are optimized and secondly, if the desorption flash that requires preheating of the feed is included to recycle the absorbent, the heat integration analysis will be a reasonable approach to increase the efficency of the process.

This work provides the framework to analyze the heat integration potential for any flowsheet in Aspen Custom Modeler® provided with implemented code described in chapter 4.9 using the Aspen Energy Analyzer.

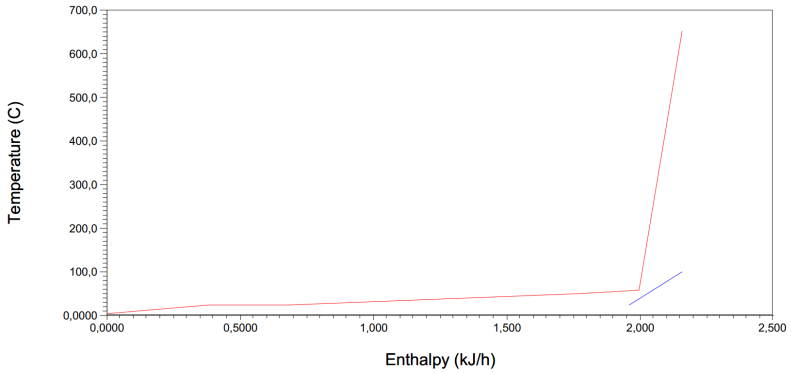

Figure 5.8: Composite curve for the PEC-PEMWE, PC, EC-COR process variant for the target value of 150 kmol/a ethylene production.

5.5 Comparison Production Target of Scale-Up Factors

In this chapter, the necessary up-scaling from the current state of the reactors to the target of 150 kg/a ethylene production is discussed for the two process variants PEC-PEMWE, PC, EC-COR firstly and secondly the for the PEC-CO2R, EC-COR. The laboratory scale setup for the EC-COR reactor is currently operated with a geometrical electrode area[1] of 10 cm^2. To achieve the desired 150 kg/a ethylene production target the EC-COR reactor required a geometrical electrode area of 933 cm^2 with a linear scaling factor of 93.3. The PEC-CO2R reactor which is designated to produce the required carbon monoxide for the EC-COR reactor produces in the current laboratory scale configuration of Boutin et al. [72] a carbon monoxide mole flow of

[1] and 32 electrolyser cells in the PEC-PEMWE reactor, which is wrongly reflected in the current state of the process flowsheet

Table 5.2: Linear scaling factors rounded to the next larger integer for the reactors used in the two process variants to achieve the desired 150 kg/a ethylene production target with the linear scaling factors for the current implementation and in the brackets, the linear scaling factors for the current laboratory states.

Variant	Scaling Factor			
	PEC-PEMWE	PC	PEC-CO2R	EC-COR
PEC-PEMWE, PC, EC-COR	10 (1)[1]	218	-	94
PEC-CO2R, EC-COR	-	-	26	94

[1] Flowsheet implemented with outdated information. Current scaling factor is one

$9.181 \cdot 10^{-5}$ kmol/h. The EC-COR demand for carbon monoxide for the desired ethylene production target is $2.53 \cdot 10^{-3}$ kmol/h. This results in a linear scaling factor of 25.8 for the PEC-CO2R reactor.

The scaling factor for the EC-COR reactor is identical with the scaling factor calculation in the previously discussed PEC-CO2R, EC-COR process variant.

The PEC-PEMWE produces a hydrogen mole flow of $7.9 \cdot 10^{-4}$ kmol/h. The inlet hydrogen flow for the PC reactor is $3.48 \cdot 10^{-5}$ kmol/h resulting in a linear scaling factor of 21.7. The PC reactor in the serially arrangement produces a component mole flow of $2.64 \cdot 10^{-4}$ kmol/h. The EC-COR demand for carbon monoxide for the desired ethylene production target is $2.53 \cdot 10^{-3}$ kmol/h resulting in a linear scaling factor of approximately 10. Thus the overall combined linear scaling factor for the PC reactor is currently 217 and the linear scaling factor for the PEC-PEMWE[2] is 10. This scaling factor results from an outdated specification and the author was informed that at the current state of the reactor, the production targets are achieved for 32 electrolyser cells in the PEC-PEMWE. In general, the last change requests from October 18, were completed on November 7. The access to all data expired on November 10. Thus, it was not possible to thoroughly check each reactor set-up and validate the data presented in this work against the data from the literature. The analysis presented in this chapter represents the current state and demonstrates the capabilities of the flowsheets and the insight that can be gained from them. The results are summarized in table 5.2 but the reactor specifications should be investigated.

It should be noted that a linear scaling of the modules is prone to errors, especially if the scaling factors are this large. Typically, the scaling of process equipment is performed with a set of dimensionless quantities to aim for physical similarity. Therefore, the scaling factors should be understood as initial scaling targets, although the actual scaling factor will most likely be larger than this.

Considering the linear scaling factors determined in this work, the PEC-CO2R, EC-COR process

[2] sufficient hydrogen for 32 electrolyser cells in the PEC-PEMWE

variant appears to be much closer to the desired ethylene production target. Under the assumption that a demonstrator system will be built with the current state of the reactors and the linear scaling factors are used to determine the number of parallel arranged reactors of each reactor kind, the PEC-PEMWE, PC, EC-COR and the PEC-CO2R, EC-COR process variant would require a total number[3] of 322 and 120 reactors. Thus, it can be confidently assumed that the PEC-CO2R, EC-COR process variant at the current stage would require less capital and operational expenditure than the PEC-PEMWE, PC, EC-COR process variant due to the much smaller number of reactors required.

[3] 312 for 32 electrolyser cells in the PEC-PEMWE

6 Summary and Outlook

The objective of the FlowPhotoChem project is the sustainable production of ethylene from carbon dioxide and water with concentrated solar irradiation as main energy input in modular reactors. To achieve this goal, three reactor modules based on different technologies were serially arranged with a photo-electrochemical proton water electrolysis reactor for the production of hydrogen, a photocatlytic reactor for the production of carbon monoxide from hydrogen and carbon dioxide, and an electrocatalytic carbon monoxide reduction reactor for the production of ethylene and unwanted byproducts. As alternative, a second process was introduced during the working period of this work with two serially arranged reactor modules, a photo-electrochemical carbon dioxide reduction reactor for the production of carbon monoxide and the electrochemical carbon monoxide reduction reactor for the production of ethylene and byproducts, which is identical to the electrochemical carbon monoxide reduction reactor in the initial process design. The objective of this was to improve and to extend the existing reactor models for Aspen Custom Modeler® , and to create flowsheets for the initially only one and later throughout this work two process variants for the current production resulting from the laboratory scale of the reactors and the ethylene production target of 150 kg/a. The linear scaling factors necessary to achieve the production target for the reactors in each process variant were calculated. The resulting scaling factors show that the process variant using the photo-electrochemical carbon dioxide reduction reactor and the electrochemical carbon monoxide reduction reactor, the process variant that was introduced as alternative concept, is at the current stage of the project closer to the ethylene production target of 150 kg/a. With respect to the maximum linear scaling factors from all reactors used in a single process variant, variant 1 must be scaled by a linear scaling factor of 217 for the photocatalytic reactor and variant 2 by a linear scaling factor of 94 for the electrochemical carbon monoxide reduction reactor demonstrating the greater progress made in the second process variant.

Furthermore, this thesis aimed to assess the heat integration potential. Heat must be removed for all operations throughout all four process variants with the exception of the pre-heating of the photocatalytic reactor, and, therefore, the heat integration potential is very limited. Within the heat integration analysis in this work, a flexible script was developed that can handle user supplied Aspen Custom Modeler® flowsheets and export all necessary data in the correct format for the use with Aspen Energy Analyzer.

Throughout the flowsheets, the electrolyser model for the electrochemical reduction of carbon dioxide and carbon monoxide is used often. Progress towards a fully temperature and pressure

dependent model has been made in this work. The reversible potential for the half cell reaction can be calculated at standard temperature and pressure with the Gibbs free energy of the hydroxide ion calculated as part of this work. A temperature dependent form of the activation overpotential equation was introduced. The parameter fitting was successful for a single temperature, but remained unsuccessful when tested against experimental data with different temperatures that were initially excluded from the fitting. In the inital parameter fit, the data set was separated in two sets, one used for the parameter fit and one used to review the model against data excluded from the parameter fit. Thus, the parameter fit was repeated with all the data currently available at the expense of not having an unused set of experimental data to test the validity of the fit. With the genetic algorithm and particleswarm, non-gradient based optimization strategies were added to the solution methods to fit the parameters. The parameter fit remained unsuccessful using both gradient-based and non gradient-based optimization algorithms. This is most likely a result of the limited experimental data available. Thus, the cathode activation overpotential for the photo-electrochemical carbon dioxide reduction reactor were fitted using a phenomenological approach for the activation overpotential. A temperature dependent equation for the concentration overpotential was introduced with a limiting current density at which diffusive mass transport falls short of the reaction rate of the electrolyser. The required equations, thermodynamic and transport model parameters were researched and presented in this work to numerically solve the diffusion problem. Using the concentration overpotential equation introduced in succeeding work can result in a calculated limiting current density. The current density limit could be determined with parameter fits and experimental data for higher current densities or with numerically solving the diffusion regime responsible for the concentration overpotential. Pursuing a fully temperature dependent electolyser model with successfully fitted model parameters for all electrolysers used throughout the project remains critical to determine the ideal operating point to increase the ethylene production efficiency and should be completed prior to the heat integration.

The simulation of the photocatalytic reactor has been peculiar. Questions were raised whether the catalytic activity is driven by photocatalytic or photo-thermal processes. While the answer to this question remains unclear, the working thesis of a photo-thermal driven reaction was adopted on the basis of reviewed literature and measured temperatures during the operation of the photocatalytic reactor. Extensive research on reaction kinetic models for the simulation of the photocatalytic reactor was concluded as part of this work. The most promising reaction kinetic models were reviewed. As a result of the literature review, reaction rate equations from Vidal-Vazquez et al. [65] were adapted and used. To gain a deeper understanding of the flow characteristics in the photocatalytic reactor, a computational fluid dynamics simulation was performed with OpenFOAM® . The results demonstrated laminar flow behavior with a channel flow in the center of the reactor and a broad residence time distribution within one order of magnitude. Furthermore, routes to model improvement were identified that leverage existing knowledge in fluid dynamics coupled with radiation heat transfer. Existing internal knowledge can be used in the next development stage to couple the convective and diffusive flow with radiation heat transfer and possibly with a surface reaction rate boundary condition including a reaction rate for the photo-driven reverse water gas shift reaction. In this work, the initial step was taken towards gaining valuable insights

in the photocatalytic reactor that should be further pursued supplementing planned experimental investigations of the photocatalytic reactor.

Additionally to the identified objectives of this work, possible processes for the removal and recycling of not reacted carbon dioxide from the product carbon monoxide stream to the electrochemical carbon monoxide reduction reactor were researched and discussed. Studies conducted by Mattirolo [102] investigating the usage of absorption, adsorption, cryogenic distillation, and membrane separation technology showed that the most often utilized separation technology is absorption based. Industrially relevant configurations and patented processes were reviewed as part of this work. The review demonstrated that carbon dioxide can be removed to almost any degree resulting in carbon monoxide purites greater than 99 %. Thus, it is only a matter of choosing the right gas separation technology since any purity requirement can be met. Two amine solutions, potassium hydroxide solution and water were compared in this work using a physical property model suitable for electrolytes and vapor-liquid-equilibrium calculations in Aspen. The final solvent selection should be made once the upstream purity requirements for the carbon monoxide feed of the electrochemical carbon monoxide reduction reactor are specified.

A Appendix Aspen Custom Modeler®

Table A.1: Design parameters for the GaInP/GaInAs/Ge triple junction concentrated Photovoltaic cell from Holmes-Gentle et al. [30].

Variable	Value	Description	Units
A_{PV}	0.000104	Area of single cell	m^2
α	0.0005771, 0.000363, 0.0005405, 0.000419, 0.0004774	Material constant for GaP, InP, GaAs, InAs, Ge	eV/K
$E_{g,0}$	2.857, 1.411, 1.519, 0.42, 0.7437	Bandgap of GaP, InP, GaAs, InAs, Ge at 0 K	eV
f_{Eg}	1.018, 1.192, 0	Bandgap correction factor for j1 & j2	1/K
γ	1.81, 1.86, 1.44	Material constants (j1, j2, j3)	-
$j_{sc,1C,298K}$	126, 127, 190	Short circuit current density at 298.15 K and 1C solar irradiation (j1, j2, j3)	A/m^2
κ	0.0001833, 0.002195, 0.19187	Material constants (j1, j2, j3)	-
μsc	0.00063, 0.00063, 0.00036	Temperature dependence coefficient for Isc (j1, j2, j3)	1/K
n	1.89, 1.59, 1.43	Diode ideality factor (j1, j2, j3)	-
N_p	4	Parallel triple junction PV cells	-
N_s	24	Serial triple junction PV cells	-
R_s	0.023	Total series resistance of all junctions	Ω
σ	372, 162, 204, 271, 235	Constant for GaP, InP, GaAs, InAs, Ge [K]	°C
C	813.8	Solar Irridiation in C = 1 sun	kW/m^2
T_{PV}	25	Cell temperature	°C
x	0.51, 0.49, 0.99, 0.01	Alloy composition In0.49Ga0.51P, In0.01Ga0.99As, Ge1	-

Table A.2: Design parameters for the CO electrolyser EC-COR without the stochiometry coefficients.

Variable	Value	Description	Units
ASR	0.5	Area specific electrical resistance of Membrane	m2
dP_loss_Anode	0	Pressure Loss in each Half Cell	bar
dP_loss_Cathode	0	Pressure Loss in each Half Cell	bar
Q_dot	0	Heat flow over solid reactor boundaries / kW	kW
dG0_Rxn	0.05		GJ/kmol
dS0_Rxn	0		kJ/kmol/K
E_rev("COR_ACETIC")	0.533		
E_rev("COR_C2H4")	0.657		
E_rev("COR_ETOH")	0.652		
E_rev("COR_PROH")	0.628		
E_rev("HER")	0.828		
E_rev("OER")	0.401		
P_0	1.013	reference pressure	bar
ParameterInocConductivity("E_a")	2	Parameters for the Inoic conductivity of the Membrane	
ParameterInocConductivity("k")	1	Parameters for the Inoic conductivity of the Membrane	
ParameterInocConductivity("sigma_0")	1	Parameters for the Inoic conductivity of the Membrane	
ParameterPhenomenological("COR_ACETIC","p1")	0.136371	Parameters for the phenomenological Model for each Halfreaction	

Table A.2: Design parameters for the CO electrolyser EC-COR without the stochiometry coefficients.

Variable	Value	Description	Units
ParameterPhenomenological("COR_ACETIC","p2")	1.0218E-08	Parameters for the phenomenological Model for each Halfreaction	
ParameterPhenomenological("COR_ACETIC","p3")	7.7221	Parameters for the phenomenological Model for each Halfreaction	
ParameterPhenomenological("COR_ACETIC","p4")	0	Parameters for the phenomenological Model for each Halfreaction	
ParameterPhenomenological("COR_ACETIC","p5")	0	Parameters for the phenomenological Model for each Halfreaction	
ParameterPhenomenological("COR_C2H4","p1")	0.130228	Parameters for the phenomenological Model for each Halfreaction	
ParameterPhenomenological("COR_C2H4","p2")	5.8155E-07	Parameters for the phenomenological Model for each Halfreaction	
ParameterPhenomenological("COR_C2H4","p3")	1.90199	Parameters for the phenomenological Model for each Halfreaction	
ParameterPhenomenological("COR_C2H4","p4")	0	Parameters for the phenomenological Model for each Halfreaction	
ParameterPhenomenological("COR_C2H4","p5")	0	Parameters for the phenomenological Model for each Halfreaction	
ParameterPhenomenological("COR_ETOH","p1")	0.140575	Parameters for the phenomenological Model for each Halfreaction	
ParameterPhenomenological("COR_ETOH","p2")	3.609E-07	Parameters for the phenomenological Model for each Halfreaction	

Table A.2: Design parameters for the CO electrolyser EC-COR without the stochiometry coefficients.

Variable	Value	Description	Units
ParameterPhenomenological("COR_ETOH","p3")	5.52518	Parameters for the phenomenological Model for each Halfreaction	
ParameterPhenomenological("COR_ETOH","p4")	0	Parameters for the phenomenological Model for each Halfreaction	
ParameterPhenomenological("COR_ETOH","p5")	0	Parameters for the phenomenological Model for each Halfreaction	
ParameterPhenomenological("COR_PROH","p1")	0.132475	Parameters for the phenomenological Model for each Halfreaction	
ParameterPhenomenological("COR_PROH","p2")	3.1127E-07	Parameters for the phenomenological Model for each Halfreaction	
ParameterPhenomenological("COR_PROH","p3")	6.20465	Parameters for the phenomenological Model for each Halfreaction	
ParameterPhenomenological("COR_PROH","p4")	0	Parameters for the phenomenological Model for each Halfreaction	
ParameterPhenomenological("COR_PROH","p5")	0	Parameters for the phenomenological Model for each Halfreaction	
ParameterPhenomenological("HER","p1")	0.131059	Parameters for the phenomenological Model for each Halfreaction	
ParameterPhenomenological("HER","p2")	4.6236E-05	Parameters for the phenomenological Model for each Halfreaction	
ParameterPhenomenological("HER","p3")	3.04963	Parameters for the phenomenological Model for each Halfreaction	

Table A.2: Design parameters for the CO electrolyser EC-COR without the stochiometry coefficients.

Variable	Value	Description	Units
ParameterPhenomenological("HER","p4")	0.0171817	Parameters for the phenomenological Model for each Halfreaction	
ParameterPhenomenological("HER","p5")	979.664	Parameters for the phenomenological Model for each Halfreaction	
ParameterPhenomenological("OER","p1")	0.0426207	Parameters for the phenomenological Model for each Halfreaction	
ParameterPhenomenological("OER","p2")	7.9011E-12	Parameters for the phenomenological Model for each Halfreaction	
ParameterPhenomenological("OER","p3")	0.120405	Parameters for the phenomenological Model for each Halfreaction	
ParameterPhenomenological("OER","p4")	0	Parameters for the phenomenological Model for each Halfreaction	
ParameterPhenomenological("OER","p5")	0	Parameters for the phenomenological Model for each Halfreaction	
T_0	24,85	reference temperature	C

B OpenFOAM®

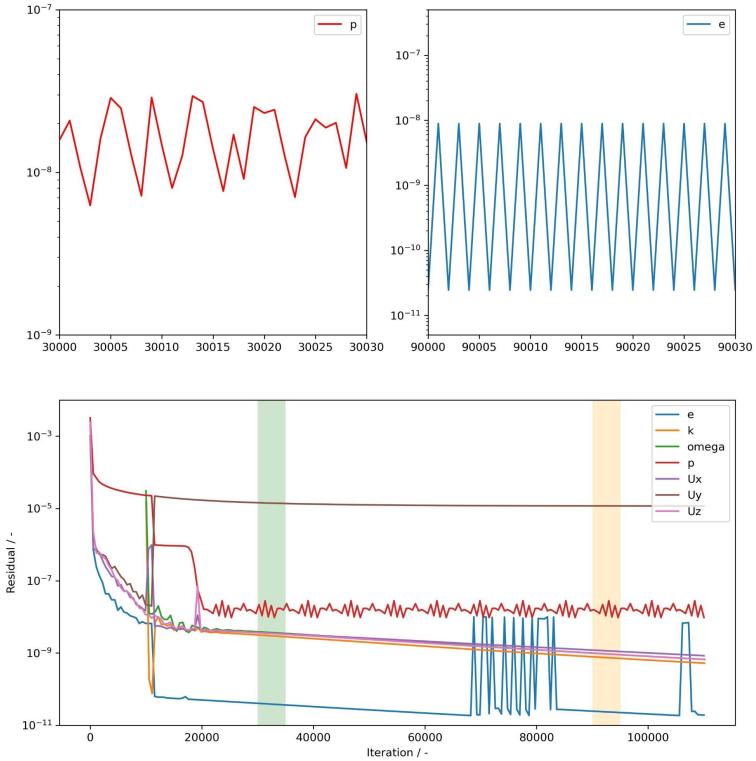

Figure B.1: Residual plots for the photocatalytic reactor CFD simulation with OpenFOAM® . The global plot shows a smoothed residual plot and the two magnifications above show the true residuals with the oscillation for e and p.

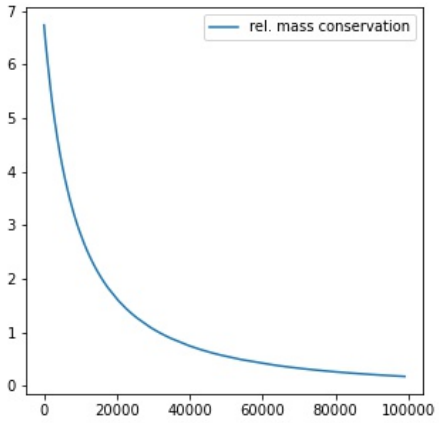

Figure B.2: Relative mass conservation for the photocatalytic reactor CFD simulation with OpenFOAM® .

Source Code B.1: OpenFOAM® Function object to log the inlet and outlet mass flux to the console. The source code shows only the function for the inlet with outlet implemented analogeously.

```
PatchMassFlowInlet                                                  1
{                                                                   2
    type                surfaceFieldValue;                          3
    writeControl        timeStep;                                   4
    writeInterval       $eWI;                                       5
    executionControl    timeStep;                                   6
    executionInterval   $eWI;                                       7
    writeFields         true;                                       8
    log                 false;                                      9
                                                                    10
    regionType          patch;                                      11
    name                inlet;                                      12
    operation           sum;                                        13
    fields              (phi);                                      14
}                                                                   15
```

Source Code B.2: Nasa7 coefficients for the Water Gas Shift Reaction

```
H2                TPIS78H   2               G   200.000       1
   3500.000  1000.000    1
 3.33727920E+00-4.94024731E-05 4.99456778E-07-1.79566394E-10   2
    2.00255376E-14    2
-9.50158922E+02-3.20502331E+00 2.34433112E+00 7.98052075E      3
   -03-1.94781510E-05    3
 2.01572094E-08-7.37611761E-12-9.17935173E+02 6.83010238E-01   4
                      4
H2O               L 8/89H   2O   1          G   200.000       5
   3500.000  1000.000    1
 3.03399249E+00 2.17691804E-03-1.64072518E-07-9.70419870E-11   6
    1.68200992E-14    2
-3.00042971E+04 4.96677010E+00 4.19864056E+00-2.03643410E-03   7
   6.52040211E-06    3
-5.48797062E-09 1.77197817E-12-3.02937267E+04-8.49032208E-01   8
                      4
CO                TPIS79C   1O   1          G   200.000       9
   3500.000  1000.000    1
 2.71518561E+00 2.06252743E-03-9.98825771E-07 2.30053008E      10
    -10-2.03647716E-14    2
-1.41518724E+04 7.81868772E+00 3.57953347E+00-6.10353680E-04   11
   1.01681433E-06    3
 9.07005884E-10-9.04424499E-13-1.43440860E+04 3.50840928E+00   12
                      4
CO2               L 7/88C   1O   2          G   200.000       13
   3500.000  1000.000    1
 3.85746029E+00 4.41437026E-03-2.21481404E-06 5.23490188E      14
    -10-4.72084164E-14    2
-4.87591660E+04 2.27163806E+00 2.35677352E+00 8.98459677E      15
   -03-7.12356269E-06    3
 2.45919022E-09-1.43699548E-13-4.83719697E+04 9.90105222E+00   16
                      4
```

C Bibliography

[1] Die Treibhausgase: UBA-Erklärfilm: Treibhausgase und Treibhauseffekt, **2022**.

[2] Treibhausgas-Emissionen in Deutschland: Treibhausgas-Emissionen nach Kategorien, **2022**.

[3] U. B. Umweltbundesamt, Treibhausgas-Emissionen in Deutschland, **2016**.

[4] Wissenschaftlicher Beirat der Bundesregierung, Factsheet Nr. 2/2011 Transformation der Energiesysteme, **2012**.

[5] Umweltbundesamt, Primärenergieverbrauch nach Energieträgern, **2022**.

[6] M. McCoy, Reisch M., A. H. Tullo, P. L. Short, *Chemical & Engineering News Archive* **2006**, *84*, 59–68.

[7] FlowPhotoChem: Sustainable Chemicals with Sunlight and CO2.

[8] R. P. O'Hayre, S.-W. Cha, W. G. Colella, F. B. Prinz, *Fuel cell fundamentals*, Third edition, Wiley, Hoboken New Jersey, **2016**.

[9] P. Perrot, *A to Z of thermodynamics*, Oxford Univ. Press, Oxford, **1998**.

[10] J. D. Cox, *Pure and Applied Chemistry* **1982**, *54*, 1239–1250.

[11] C. S. Helrich, *Modern Thermodynamics with Statistical Mechanics*, Springer Berlin Heidelberg, Berlin, Heidelberg, **2008**.

[12] P. Atkins, J. de Paula, *Termodynamics and kinetics*, 8th ed., W.H. Freeman and Co, New York, **2005**.

[13] F. P. Incropera, D. P. Dewitt, *Fundamentals of heat and mass transfer*, 3rd ed., Wiley, New York [etc.], **1990**.

[14] S. V. Patankar, *Numerical heat transfer and fluid flow*, Taylor & Francis, Bristol, Pa., **1980**.

[15] C. J. Greenshields et al., *OpenFOAM Foundation Ltd version* **2015**, *3*, 47.

[16] *Statistical mechanics*, 3rd ed., (Ed.: R. K. Pathria), Elsevier/Academic Press, Amsterdam and Boston, **2011**.

[17] J. O. Hirschfelder, C. F. Curtiss, R. B. Bird, *Molecular theory of gases and liquids*, Corr. print. with notes added., Wiley, New York,NY, **1964**.

[18] G. P. Smith, GRI-Mech 3.0, **1999**.

[19] M. Klein, F. J. Smith, *Journal of Research of the National Bureau of Standards. Section A Physics and Chemistry* **1968**, *72*, 359.

[20] R. E. Swaney, R. B. Bird, *Physics of Fluids* **2019**, *31*, 021202.

[21] N. Epstein, *Chemical Engineering Science* **1989**, *44*, 777–779.

[22] C. Zhang, J. Zhang, X. Ma, Q. Feng, *Semiconductor Photovoltaic Cells*, 1st ed. 2021, Springer Singapore and Imprint Springer, Singapore, **2021**.

[23] M. Balkanski, R. F. Wallis, *Semiconductor physics and applications*, Reprinted., Oxford Univ. Press, Oxford, **2008**.

[24] *Thermodynamics of Energy Conversion and Transport*, (Eds.: S. Sieniutycz, A. Vos), Springer New York, New York, NY and s.l., **2000**.

[25] J. Bartlett, *Electronics for Beginners: A Practical Introduction to Schematics, Circuits, and Microcontrollers*, 1st edition, Apress and Safari, Erscheinungsort nicht ermittelbar and Boston, MA, **2020**.

[26] G. Segev, G. Mittelman, A. Kribus, *Solar Energy Materials and Solar Cells* **2012**, *98*, 57–65.

[27] *Handbook of photovoltaic science and engineering*, (Ed.: A. Luque López), Wiley, New York and Chichester, **2003**.

[28] Y. P. Varshni, *Physica* **1967**, *34*, 149–154.

[29] I. Vurgaftman, J. R. Meyer, L. R. Ram-Mohan, *Journal of Applied Physics* **2001**, *89*, 5815–5875.

[30] I. Holmes-Gentle, S. Tembhurne, C. Suter, S. Haussener, *International Journal of Hydrogen Energy* **2021**, *46*, 10666–10681.

[31] *Hydrogen production: By electrolysis*, 1st edition, (Eds.: A. Godula-Jopek, D. Stolten), Wiley-VCH, Weinheim, **2015**.

[32] J. C. Garcia-Navarro, M. Schulze, K. A. Friedrich, *Journal of Power Sources* **2019**, *431*, 189–204.

[33] D. Chattopadhyay, P. S. Rakshit, *Electronics: fundamentals and applications*, 7th ed., New Age Publishers, New Delhi, **2006**.

[34] R. Memming, *Semiconductor electrochemistry*, Second edition, Wiley-VCH, Weinheim, **2015**.

[35] H. I. de Lasa, B. Serrano, M. Salaices, *Photocatalytic reaction engineering*, Springer Science+Business Media, LLC, New York, **2010**.

[36] S. N. Habisreutinger, L. Schmidt-Mende, J. K. Stolarczyk, *Angewandte Chemie (International ed. in English)* **2013**, *52*, 7372–7408.

[37] *Fluidverfahrenstechnik: Grundlagen, Methodik, Technik, Praxis*, (Ed.: R. Goedecke), Wiley-VCH, Weinheim, **2006**.

[38] M. Baerns, A. Behr, A. Brehm, J. Gmehling, K.-O. Hinrichsen, H. Hofmann, R. Palkovits, U. Onken, A. Renken, *Technische Chemie*, Zweite, erweiterte Auflage, Wiley-VCH and Ciando, Weinheim and München, **2013**.

[39] A. K. Coker, *Ludwig's applied process design for chemical and petrochemical plants*, *Vol. 2*, 4th ed., Elsevier Gulf Professional Publ, Amsterdam, **2010**.

[40] X.-S. Yang, *Nature-inspired optimization algorithms*, Second edition, Academic Press, London and San Diego, CA, **2021**.

[41] *Optimization for Data Analysis*, (Eds.: S. J. Wright, B. Recht), Cambridge University Press, **2022**.

[42] Bhandari P., Random vs. Systematic Error | Definition & Examples, **2022**.

[43] P. K. Mogensen, A. N. Riseth, *Journal of Open Source Software* **2018**, *3*, 615.

[44] J. Bezanson, A. Edelman, S. Karpinski, V. B. Shah, *SIAM Review* **2017**, *59*, 65–98.

[45] *Brain Storm Optimization Algorithms: Concepts, Principles and Applications*, (Eds.: S. Cheng, Y. Shi), Springer, Cham, **2019**.

[46] Evolutionary.jl.

[47] P. B. Borckmans, M. Ishteva, P.-A. Absil in *Swarm Intelligence*, (Eds.: D. Hutchison, T. Kanade, J. Kittler, J. M. Kleinberg, F. Mattern, J. C. Mitchell, M. Naor, O. Nierstrasz, C. Pandu Rangan, B. Steffen, M. Sudan, D. Terzopoulos, D. Tygar, M. Y. Vardi, G. Weikum, M. Dorigo, M. Birattari, G. A. Di Caro, R. Doursat, A. P. Engelbrecht, D. Floreano, L. M. Gambardella, R. Groß, E. Şahin, H. Sayama, T. Stützle), Lecture Notes in Computer Science, Springer Berlin Heidelberg, Berlin, Heidelberg, **2010**, pp. 13–23.

[48] N. Boumal, B. Mishra, P.-A. Absil, R. Sepulchre, *Journal of Machine Learning Research* **2014**, *15*, 1455–1459.

[49] M. M. Khan, *Nanocomposites for Visible Light-induced Photocatalysis*, Springer International Publishing, Cham, **2017**.

[50] C.-C. Yang, Y.-H. Yu, B. van der Linden, J. C. S. Wu, G. Mul, *Journal of the American Chemical Society* **2010**, *132*, 8398–8406.

[51] T. Yui, A. Kan, C. Saitoh, K. Koike, T. Ibusuki, O. Ishitani, *ACS applied materials & interfaces* **2011**, *3*, 2594–2600.

[52] R. Carrasquillo-Flores, I. Ro, M. D. Kumbhalkar, S. Burt, C. A. Carrero, A. C. Alba-Rubio, J. T. Miller, I. Hermans, G. W. Huber, J. A. Dumesic, *Journal of the American Chemical Society* **2015**, *137*, 10317–10325.

[53] C.-.-S. Chen, W.-.-H. Cheng, S.-.-S. Lin, *Catalysis Letters* **2000**, *68*, 45–48.

[54] V. D. Dasireddy, D. Vengust, B. Likozar, J. Kovač, A. Mrzel, *Renewable Energy* **2021**, *176*, 251–261.

[55] Y. A. Daza, J. N. Kuhn, *RSC Advances* **2016**, *6*, 49675–49691.

[56] M. Gu, S. Dai, R. Qiu, M. E. Ford, C. Cao, I. E. Wachs, M. Zhu, *ACS Catalysis* **2021**, *11*, 12609–12619.

[57] N. Ishito, K. Hara, K. Nakajima, A. Fukuoka, *Journal of Energy Chemistry* **2016**, *25*, 306–310.

[58] B. Liang, H. Duan, X. Su, X. Chen, Y. Huang, X. Chen, J. J. Delgado, T. Zhang, *Catalysis Today* **2017**, *281*, 319–326.

[59] X. Liu, P. La Ramírez de Piscina, J. Toyir, N. Homs, *Catalysis Today* **2017**, *296*, 181–186.

[60] A. A. Upadhye, I. Ro, X. Zeng, H. J. Kim, I. Tejedor, M. A. Anderson, J. A. Dumesic, G. W. Huber, *Catalysis Science & Technology* **2015**, *5*, 2590–2601.

[61] C. A. Callaghan, *Kinetics and catalysis of the water-gas-shift reaction: A microkinetic and graph theoretic approach*, Worcester Polytechnic Institute, **2006**.

[62] Y. Dubi, I. W. Un, Y. Sivan, *Chemical science* **2020**, *11*, 5017–5027.

[63] J. Xu, G. F. Froment, *AIChE Journal* **1989**, *35*, 88–96.

[64] J. Xu, G. F. Froment, *AIChE Journal* **1989**, *35*, 97–103.

[65] F. Vidal Vázquez, P. Pfeifer, J. Lehtonen, P. Piermartini, P. Simell, V. Alopaeus, *Industrial & Engineering Chemistry Research* **2017**, *56*, 13262–13272.

[66] S. S. Kim, H. H. Lee, S. C. Hong, *Applied Catalysis A: General* **2012**, *423-424*, 100–107.

[67] L. Zhang, L. Chen, S. Xia, C. Wang, F. Sun, *Entropy (Basel Switzerland)* **2018**, *20*, DOI `\url{10.3390/e20060415}`.

[68] J. A. Hernandez Lalinde, P. Roongruangsree, J. Ilsemann, M. Bäumer, J. Kopyscinski, *Chemical Engineering Journal* **2020**, *390*, 124629.

[69] Guide for the verification and validation of computational fluid dynamics simulations, Reston, Va., **1998**.

[70] J. C. Bui, E. W. Lees, L. M. Pant, I. V. Zenyuk, A. T. Bell, A. Z. Weber, *Chemical reviews* **2022**, *122*, 11022–11084.

[71] B. Endrődi, A. Samu, E. Kecsenovity, T. Halmágyi, D. Sebők, C. Janáky, *Nature energy* **2021**, *6*, 439–448.

[72] E. Boutin, M. Patel, E. Kecsenovity, S. Suter, C. Janáky, S. Haussener, *Advanced Energy Materials* **2022**, *12*, 2200585.

[73] B. Endrődi, E. Kecsenovity, A. Samu, T. Halmágyi, S. Rojas-Carbonell, L. Wang, Y. Yan, C. Janáky, *Energy & Environmental Science* **2020**, *13*, 4098–4105.

[74] M. Suermann, T. J. Schmidt, F. N. Büchi, *Electrochimica Acta* **2016**, *211*, 989–997.

[75] N. S. Romero Cuellar, C. Scherer, B. Kaçkar, W. Eisenreich, C. Huber, K. Wiesner-Fleischer, M. Fleischer, O. Hinrichsen, *Journal of CO2 Utilization* **2020**, *36*, 263–275.

[76] G. F. Froment, K. B. Bischoff, *Chemical reactor analysis and design*, 2. ed., Wiley, New York, **1990**.

[77] *Mathematical aspects of numerical grid generation: "Based on the papers presented at the two minisymposia, "Numerical grid generation : mathematical aspects, parts I and II," held at the SIAM Annual Meeting in Minneapolis, Minnesota, in July 1988"–Pref*, Society for Industrial and Applied Mathematics (SIAM 3600 Market Street Floor 6 Philadelphia PA 19104), Philadelphia, Pa, **1991**.

[78] F. Liu, *Proceedings of CFD with OpenSource Software* **2016**, *34*.

[79] S. M. Salim, S. Cheah in Proceedings of the international multiconference of engineers and computer scientists, *Vol. 2*, **2009**, pp. 2165–2170.

[80] S. B. Pope, *Turbulent Flows*, Cambridge University Press, **2012**.

[81] L. Prandtl, *ZAMM - Journal of Applied Mathematics and Mechanics / Zeitschrift für Angewandte Mathematik und Mechanik* **1925**, *5*, 136–139.

[82] F. Menter in 23rd Fluid Dynamics, Plasmadynamics, and Lasers Conference, (Ed.: F. Menter), American Institute of Aeronautics and Astronautics, Reston, Virigina, **1993**.

[83] C. J. Greenshields, *The OpenFOAM Foundation* **2018**, *237*.

[84] H. S. Fogler, *Elements of chemical reaction engineering*, Sixth edition, Pearson, Boston et al., **2020**.

[85] Prognos AG, Energiewirtschaftliches Institut an der Universität zu Köln, Gesellschaft für wirtschaftliche Strukturforschung, Entwicklung der Energiemärkte – Energiereferenzprognose: Studie im Auftrag des Bundesministeriums für Wirtschaft und Technologie: Projekt Nr. 57/12, **2014**.

[86] P. J. Linstrom, W. G. Mallard, *Journal of Chemical & Engineering Data* **2001**, *46*, 1059–1063.

[87] JANAF Thermochemical Tables.

[88] E. Favre, *Journal of Membrane Science* **2007**, *294*, 50–59.

[89] U. Ali, E. O. Agbonghae, K. J. Hughes, D. B. Ingham, L. Ma, M. Pourkashanian, *Applied Thermal Engineering* **2016**, *103*, 747–758.

[90] G. Cau, V. Tola, F. Ferrara, A. Porcu, A. Pettinau, *Fuel* **2018**, *214*, 423–435.

[91] Y. Hu, G. Xu, C. Xu, Y. Yang, *Applied Thermal Engineering* **2017**, *111*, 308–316.

[92] K. Li, W. Leigh, P. Feron, H. Yu, M. Tade, *Applied Energy* **2016**, *165*, 648–659.

[93] M. Micari, M. Dakhchoune, K. V. Agrawal, *Journal of Membrane Science* **2021**, *624*, 119103.

[94] P. Panja, B. McPherson, M. Deo, *Carbon Capture Science & Technology* **2022**, *3*, 100041.

[95] A. Rolfe, Y. Huang, M. Haaf, S. Rezvani, A. Dave, N. J. Hewitt, *Energy Procedia* **2017**, *142*, 3447–3453.

[96] S. Roussanaly, A. L. Brunsvold, E. S. Hognes, J. P. Jakobsen, X. Zhang, *Energy Procedia* **2013**, *37*, 2453–2461.

[97] M.-O. Schach, R. Schneider, H. Schramm, J.-U. Repke, *Industrial & Engineering Chemistry Research* **2010**, *49*, 2363–2370.

[98] D. Singh, E. Croiset, P. Douglas, M. Douglas, *Energy Conversion and Management* **2003**, *44*, 3073–3091.

[99] M. van der Spek, E. Sanchez Fernandez, N. H. Eldrup, R. Skagestad, A. Ramirez, A. Faaij, *International Journal of Greenhouse Gas Control* **2017**, *56*, 221–236.

[100] M. Kargol, J. Zajac, D. J. Jones, J. Rozière, A. B. Jarzębski in *Characterization of Porous Solids VII - Proceedings of the 7th International Symposium on the Characterization of Porous Solids (COPS-VII), Aix-en-Provence, France, 26-28 May 2005*, Studies in Surface Science and Catalysis, Elsevier, **2007**, pp. 357–364.

[101] A. Keller, R. Schendel, **1988**.

[102] P. Mattirolo, **2012**.

[103] M. Mintz, J. Han, A. Burnham in *Alternative Fuels and Advanced Vehicle Technologies for Improved Environmental Performance*, Elsevier, **2014**, pp. 90–116.

[104] Robert D. Hughes, Edward F., 3823529, **July 16, 1974**.

[105] H. Genroku Nakao, K. Hiroshi Ishisaka, Shigehito Takamoto, Yasuyuki Nishimura, 4,950,462, **Aug. 21, 1990**.

[106] M. Appl, U. Wagner, H. J. Henrici, K. Kuessner, K. Volkamer, E. Fuerst, 4,336,233, **Jun. 22, 1982**.

[107] A. L. Kohl, R. B. Nielsen, *Gas purification*, 5. ed., Gulf Publ. Co, Houston, Tex., **1997**.

[108] Z. Duan, R. Sun, *Chemical Geology* **2003**, *193*, 257–271.

Declaration

The submitted thesis was supervised by Prof. Dr.-Ing. Kai-Olaf Hinrichsen.

Affirmation
Hereby, I affirm that I am the sole author of this thesis. To the best of my knowledge, I affirm that this thesis does not infringe upon anyone's copyright nor violate any proprietary rights. I affirm that any ideas, techniques, quotations, or any other material, are in accordance with standard referencing practices.

Moreover, I affirm that, so far, the thesis has not been forwarded to a third party nor is it published. I obeyed all study regulations of the Technische Universität München.

Remarks about the internet
Throughout the work, the internet was used for research and verification. Many of the keywords provided herein, references and other information can be verified on the internet. However, no sources are given, because all statements made in this work are fully covered by the cited literature sources.

Garching, November 19, 2022

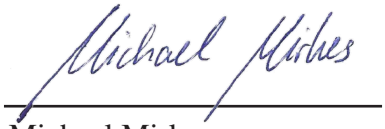

Michael Mirkes